# Computational modelling of structural batteries accounting for stress-assisted convection in the electrolyte



Citation for the original published paper (version of record):
Carlstedt, D., Runesson, K., Larsson, F. et al (2022). Computational modelling of structural batteries accounting for stress-assisted convection in
the electrolyte. International Journal of Solids and Structures, 238.
http://dx.doi.org/10.1016/j.ijsolstr.2021.111343



(article starts on next page)

International Journal of Solids and Structures 238 (2022) 111343

Contents lists available at ScienceDirect

International Journal of Solids and Structures

journal homepage: www.elsevier.com/locate/ijsolstr

# Computational modelling of structural batteries accounting for stress-assisted convection in the electrolyte

David Carlstedt [a,*], Kenneth Runesson [a], Fredrik Larsson [a], Vinh Tu [a], Ralf Jänicke [b], Leif E. Asp [a]

[a] Department of Industrial and Materials Science, Chalmers University of Technology, SE-412 96, Gothenburg, Sweden
[b] Institute of Applied Mechanics, Technische Universität Braunschweig, D-38106, Braunschweig, Germany

ARTICLE INFO

*Keywords:*
Li-ion based structural batteries
Porous material
Electro-chemo-mechanical processes
Stress-assisted convection
Finite Element Analysis (FEA)

ABSTRACT

Structural batteries consist of carbon fibres embedded in a porous structural battery electrolyte (SBE), which is composed of two continuous phases: a solid polymer skeleton and a liquid electrolyte containing Li-salt. In this paper we elaborate on a computational modelling framework to study the electro-chemo-mechanical properties of such structural batteries while accounting for the combined action from migration as well as stress-assisted diffusion and convection in the electrolyte. Further, we consider effects of lithium insertion in the carbon fibres, leading to insertion strains. The focus is placed on how the convective contribution to the mass transport within the SBE affects the general electro-chemo-mechanical properties. The numerical results indicate that the convective contribution has only minor influence on the multifunctional performance when the mechanical loading is caused by constrained deformation of constituents during electro-chemical cycling. However, in the case of externally applied mechanical loading that causes severe deformation of the SBE, or when large current pulses are applied, the convective contribution has noticeable influence on the electro-chemical performance. In addition, it is shown that the porosity of the SBE, which affects the effective stiffness as well as the mobility and permeability, has significant influence on the combined mechanical and electro-chemical performance.

## 1. Introduction

A trivial observation is that Li-ion based batteries are currently the dominating solution for energy storage in electrical vehicles, see e.g. Cano et al. (2018). A well-known disadvantage of the classical battery design is its large weight (or small energy to weight ratio). In order to reduce weight, significant effort has been spent in recent years to develop a concept that is coined *structural battery*, Asp et al. (2019), Thomas and Qidwai (2004), Liu et al. (2009), Johannisson et al. (2018), Ladpli et al. (2019), Moyer et al. (2020) and Zhao et al. (2020), which has the ability to simultaneously carry mechanical loads while storing electro-chemical energy. Indeed, by combining these functionalities, the structural battery offers significant system mass and volume savings (Carlstedt and Asp, 2020; Asp and Greenhalgh, 2014; Wetzel, 2004; Snyder et al., 2015; Johannisson et al., 2019).

An efficient microstructural design is offered by the *laminated structural battery* architecture, which was first proposed by Wetzel (2004) and later demonstrated by Ekstedt et al. (2010) and Carlson (2013). In the laminated battery design, laminae with different functionalities (e.g. electrodes, separator, etc.) are stacked into a laminate. In a recent study (Asp et al., 2021), the authors demonstrated a laminated structural battery with unprecedented multifunctional performance (i.e. combined electro-chemo-mechanical performance). This material featured an energy density of 24 Wh $kg^{-1}$ (at low currents) and an elastic modulus of 25 GPa.

A schematic illustration of the laminated structural battery is shown in Fig. 1a. The negative and positive electrodes are made from carbon fibres and coated carbon fibres, respectively, embedded in a Structural Battery Electrolyte (SBE) (Ihrner et al., 2017; Schneider et al., 2019) matrix. The SBE is a bi-continuous bi-phasic composite that consists of a porous polymer network (nano-scale porosity) with an open pore system saturated with the liquid electrolyte, as schematically illustrated in Fig. 1b. Clearly, the solid phase makes it possible to distribute mechanical loads, while the liquid phase enables ion transport between the electrodes.

Due to their favourable mechanical and electro-chemical properties, carbon fibres are well suited for multifunctional applications (Fredi et al., 2018; Kjell et al., 2011). The carbon fibres in the positive electrode are coated with lithium metal oxide or olivine based particles, e.g. $LiFePO_4$, binder and conductive additives (cf. Hagberg et al.

* Corresponding author.
*E-mail address:* david.carlstedt@chalmers.se (D. Carlstedt).

https://doi.org/10.1016/j.ijsolstr.2021.111343
Received 31 May 2021; Received in revised form 6 October 2021; Accepted 3 November 2021
Available online 2 December 2021

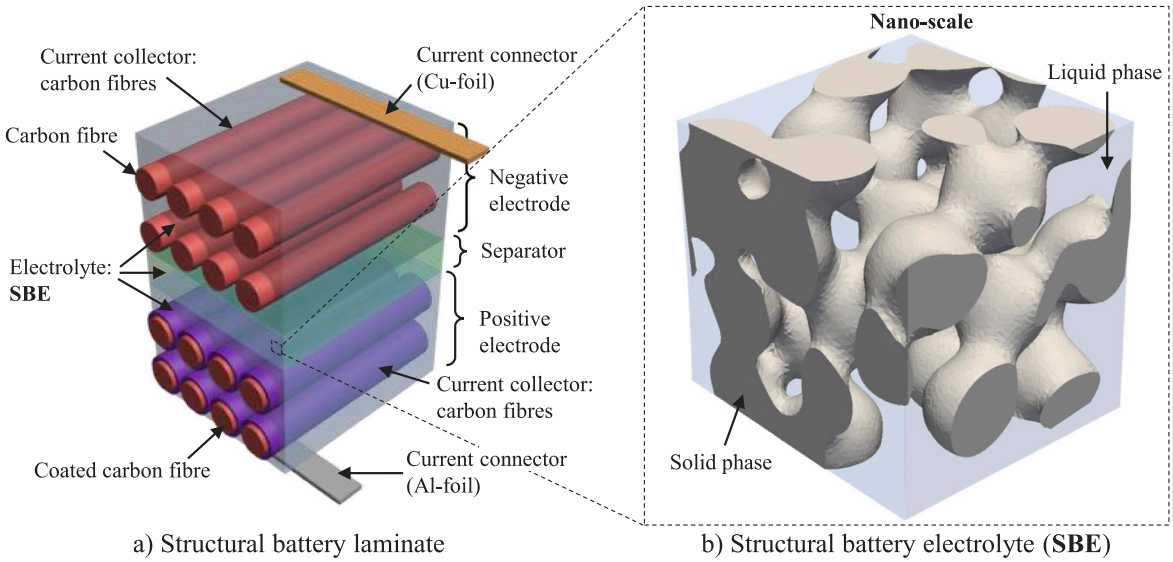


**Fig. 1.** (a) Schematic illustration of the laminated structural battery. (b) Numerically generated porous bi-continuous nano-structure, from Tu et al. (2020), representing an idealized fine-scale geometry of the Structural Battery Electrolyte (SBE) that consists of a polymer skeleton (solid phase) saturated with a liquid electrolyte phase (nano-scale porosity).

(2018)), and the two electrodes are separated by an electrically insulating layer (e.g. made from a thin layer of SBE). Finally, it is noted that the fibres in the negative electrode and the particles in the coating in the positive electrode are the active electrode materials (i.e. hosts for the lithium) in the structural battery cell.

During operation the electrode materials will expand or shrink due to insertion or de-insertion of Li-ions, and the battery cell will be exposed to external mechanical loads. For example, carbon fibres may expand up to 1% in the longitudinal direction at slow charge rate, see e.g. Jacques et al. (2013a). Hence, the porous structure of the SBE will be subjected to deformation and a pore pressure gradient that will act as the driving force for seepage of the liquid electrolyte.

As to the theoretical modelling of the multifunctional performance, structural batteries have much in common with conventional Li-ion batteries. Among the wealth of literature, we note important seminal contributions by Newman and co-workers (Newman and Tiedemann, 1975; Doyle et al., 1993; Doyle and Newman, 1995; Newman and Thomas-Alyea, 2004). In the context of electro-chemo-mechanical modelling of conventional batteries, i.e. particle based electrode materials with either liquid or solid-state electrolytes, we mention Purkayastha and Mcmeeking (2012), Bucci et al. (2016, 2017), Wu and Lu (2017, 2019), Ganser et al. (2019a,b), Wan and Ciucci (2020), Grazioli et al. (2016, 2019b,a), Bower et al. (2011), Hofmann et al. (2020), and Xu et al. (2019), to mention a few. Further, we note the work on multi-scale and computational homogenization approaches for modelling conventional Li-ion battery cells (utilizing liquid electrolyte) by Salvadori et al. (2014, 2015a,b). Notably, the convective flow of liquid electrolyte in porous electrodes should be accounted for, e.g. Xu and Zhao (2015) or Esan et al. (2020). Hence, one may favourably apply the same conceptual model framework to structural batteries while keeping in mind that the main differences are: (i) Carbon fibres (with anisotropic properties) are used as active electrode material in the negative electrode and as current collectors in both electrodes; (ii) A porous structural battery electrolyte (SBE) is used (instead of conventional liquid or solid-state electrolyte). To capture the porous nature of the SBE, stress-assisted convection, i.e. seepage of the liquid phase, in the SBE needs to be accounted for.

The importance of various interactions between the electro-chemical, thermal and mechanical fields in structural batteries have been investigated by the authors (Carlstedt et al., 2019; Carlstedt and Asp, 2019) and by Xu et al. (2018a,b), when the battery is subjected to galvanostatic cycling in terms of charging/discharging. These studies are, however, limited to one-way coupling between the electro-chemical and mechanical response and simplified geometries were studied. Tu et al. (2020) have studied the bifunctional performance of SBEs on the nano-scale, cf. Fig. 1b, while assuming linear constitutive relations for elastic stiffness and ionic conductivity. Further, Yin et al. (2020) have studied carbon fibre electrode half-cells using conventional liquid electrolyte and modified carbon fibres. Only recently, the authors (Carlstedt et al., 2020) developed a thermodynamically consistent modelling approach to study the electro-chemo-mechanical properties of structural batteries while allowing for two-way coupling between the electro-chemical and mechanical fields. It was revealed that it is vital to account for the two-way coupling in order to accurately predict the multifunctional performance of structural batteries. However, the contribution to the ion transport from convection, i.e. from seepage of the liquid phase of the SBE, was not accounted for. To date no attempt to evaluate how the pore structure/porosity of the SBE affects the electro-chemo-mechanical properties of the structural battery has been published (to the authors' knowledge).

In this paper, we take a further step towards solving the complete multiphysics problem for the laminated structural battery cell by extending the previously developed (thermodynamically consistent) theoretical framework (Carlstedt et al., 2020) to consider the porous structure of the SBE. The relevant electric, chemical and mechanical fields are thus resolved while accounting for the seepage of the liquid electrolyte in the bi-continuous polymer network of the SBE. We utilize the developed framework to solve the coupled electro-chemo-mechanical problem for a realistic conceptual microstructure and the appropriate interface and boundary conditions. Moreover, we account for the highly anisotropic behaviour of the fibres in the longitudinal and radial directions (transverse isotropy). Finally, by employing the general computational framework for analysis of the studied material, our main objectives are (i) to investigate the importance of accounting for seepage of the liquid electrolyte within the SBE and (ii) to evaluate how the pore structure/porosity of the SBE affects the electro-chemo-mechanical properties of the structural battery.

The paper is organized as follows: In Section 2, we present the conceptual microstructure and simplified architecture of the laminated structural battery cell. In Section 3, we present the governing equations for the individual domains of interest (fibre, electrolyte) for the simplified problem of the negative half-cell, as well as interface and boundary conditions, while accounting for the stress assisted convection in the SBE. Further, interpolation expressions are formulated to estimate the

effective (microscopic) properties of the SBE as function of its porosity based on computational homogenization utilizing artificially generated Representative Volume Elements (RVEs). Small strain kinematics is adopted since the considered loading will cause only small strain levels. In Section 4, we present the complete formulation of the *potentiostatic* and *galvanostatic* problems in the context of the time-incremental weak format. In Section 5, we describe the numerical implementation, including mechanical loading conditions and material properties, and in Section 6 we present the numerical results. Finally, concluding remarks and outlook to future work are presented in Section 7.

## 2. Conceptual microstructure and simplified architecture

In this paper, we study the so-called laminated structural battery cell. The conceptual microstructure of the material is illustrated in Fig. 2a. In the laminated design, the individual laminae provide different functions and are stacked into a laminate to achieve mechanical properties similar to those of conventional fibre reinforced polymer composites while providing an efficient battery function. The battery components are identified as follows: (i) The negative electrode (upper lamina in Fig. 2a). This electrode/lamina consists of carbon fibres embedded in a porous matrix (SBE); (ii) The positive electrode (lower lamina in Fig. 2a). This electrode/lamina consists of carbon fibres, coated with a mixture containing Li-metal-oxide or olivine based particles (such as $LiFePO_4$) and conductive additives (see Fig. 2b), embedded in SBE; (iii) Separator/SBE (middle lamina in Fig. 2a). This lamina assures that the active electrode materials do not come in contact, and is assumed to be made from SBE.

As discussed in previous work by the authors (Carlstedt et al., 2020), it is possible to simplify the theoretical analysis and experimental investigation of the laminated structural battery cell by using the similarity of the two electrodes in the laminated architecture (both the negative and positive electrodes consist of fibres embedded in a SBE-based matrix material). Hence, we consider the conceptual design of the negative half-cell in Fig. 2c. This battery cell corresponds to the battery cell studied in previous works (Johannisson et al., 2018; Ihrner et al., 2017; Schneider et al., 2019; Carlstedt et al., 2020). In the negative half-cell, the positive electrode in the full-cell is replaced by a collector of solid Li-metal. Further, we exclude the separator to simplify the analysis.[1] The generic/idealized model representation of this negative half-cell, which is shown in Fig. 2c, corresponds to a repeatable unit in the horizontal direction of the negative electrode lamina as illustrated in Fig. 2a (where the height of the unit corresponds to the height of the negative electrode). It should be noted that the electric potential is assumed constant along the fibres. This assumption is reasonable for battery design with short current path along the fibres (cf. Asp et al. (2021), Johannisson et al. (2018)), although the electric resistivity of the fibres is large compared with e.g. a conventional copper foil collector.

## 3. Time-continuous strong format — Individual domains, interfaces and boundaries

The time-continuous strong format and modelling assumptions for the individual domains, interfaces and boundaries are presented in this section (in accordance with previous work by the authors (Carlstedt et al., 2020)) and extended to account for stress assisted convection in the SBE. Further, the charge balance (Gauss law) is reformulated as compared to Carlstedt et al. (2020). Isothermal conditions are assumed, i.e. the absolute temperature $\theta(\boldsymbol{x},t) = \theta_0$ is only a given parameter. With respect to mechanical properties, the material response of both the carbon fibres and the SBE skeleton are assumed to be linear (i.e. linear elastic material response). With respect to the electro-chemical response on the other hand, nonlinearities are considered. Moreover, self-weight and any piezoelectric effects are ignored.

### 3.1. Fibre domain(s) $\Omega_f = \cup_i^{N_{fibres}} \Omega_{f,i}$

#### 3.1.1. Preliminaries

For the fibre domains(s) we introduce the following special assumptions: (i) Material properties are characterized as transversely isotropic, whereby isotropy pertains to the cross-section (Cartesian coordinates $x_1, x_2$); (ii) Li is the single active species, which can move into the fibre; (iii) The current between the fibres ($\Omega_f$) and the positive connector ($\Gamma_+$) is caused by electron transport in an external circuit. All fibres are connected to a collector with the *same* potential $\Phi^-(t)$, i.e. the potential is assumed uniform, $\varphi(\boldsymbol{x},t) = \Phi^-(t)$, for $\boldsymbol{x} \in \Omega_f = \cup_i^{N_{fibres}} \Omega_{f,i}$. Consequently, the electric field can be neglected and the current is therefore not resolved in the fibres (Fig. 2c).

#### 3.1.2. Balance equations for fibres

The governing balance equations in the fibre domain(s) in the strong format are summarized as follows:

$$-\boldsymbol{\sigma} \cdot \boldsymbol{\nabla} = \boldsymbol{0} \text{ in } \Omega_f \times \mathbb{R}^+ \tag{1a}$$

$$\rho \partial_t c_{Li} + \boldsymbol{j}_{Li} \cdot \boldsymbol{\nabla} = 0 \text{ in } \Omega_f \times \mathbb{R}^+ \tag{1b}$$

where $\boldsymbol{\sigma}$ is the (symmetric) stress tensor, $\boldsymbol{j}_{Li}$ is the ion flux vector for Li and $c_{Li}$ is the ion concentration of Li.[2] Finally, $\rho$ is the fibre density.

#### 3.1.3. Constitutive relations for fibres

The relevant constitutive relations are:

$$\boldsymbol{\sigma} = \mathbf{E} : \left[\boldsymbol{\epsilon}[\boldsymbol{u}] - \boldsymbol{\epsilon}^{ch}(c_{Li})\right] \tag{2a}$$

$$\boldsymbol{j}_{Li} = -\boldsymbol{M}_{Li} \cdot \boldsymbol{\nabla} \mu_{Li} \tag{2b}$$

$$\text{where } \mu_{Li} = \mu_{Li}^{en}(\boldsymbol{\epsilon}, c_{Li}) := -\rho^{-1} \boldsymbol{\alpha}^{ch} : \boldsymbol{\sigma}(\boldsymbol{\epsilon}, c_{Li}) + \mu_{Li}^0 + R\theta_0 \log\left(\frac{\tilde{c}_{Li}}{1-\tilde{c}_{Li}}\right) \tag{2c}$$

where $\boldsymbol{\epsilon}[\boldsymbol{u}]$ is the (small) strain tensor expressed as a linear operator of the displacement field $\boldsymbol{u}$. Further, $\mu_{Li}$ is the chemical potential for Li in the fibres, and its definition is based on the activity coefficient for an ideal solid solution of non-interacting particles on a lattice (cf. Bazant Bazant (2014)). In Eq. (2c), we introduce $\mu_{Li}^{en}(\boldsymbol{\epsilon}, c_{Li})$ as the explicit (energetic) relation for the chemical potential. Furthermore, $\tilde{c}_{Li}$ is the normalized ion concentration of Li w.r.t. its theoretically maximal concentration[3] (in any point in space–time), $c_{Li,max}$, thus defined as $\tilde{c}_{Li} = \frac{c_{Li}}{c_{Li,max}}$. The insertion tensor $\boldsymbol{\alpha}^{ch}$ is a second order tensor containing the transversely isotropic coefficients of the insertion induced expansion of the fibres. Further, $\mu_{Li}^0$ is a reference/standard value, $R$ is the universal gas constant and $\theta_0$ is a reference temperature.

Further, we introduced the elasticity tensor that is pertinent to transverse isotropy (which is defined by five independent parameters) as follows:

$$\begin{aligned}\mathbf{E} = {} & L_\perp \boldsymbol{I} \otimes \boldsymbol{I} + 2G_\perp \mathbf{I}^{sym} + [L_\parallel - L_\perp][\boldsymbol{I} \otimes \boldsymbol{E}_3 + \boldsymbol{E}_3 \otimes \boldsymbol{I}] \\ & + [H_\parallel - 4G_\parallel + 2G_\perp - 2L_\parallel + L_\perp]\boldsymbol{E}_3 \otimes \boldsymbol{E}_3 + 4[G_\parallel - G_\perp]\mathbf{A}\end{aligned} \tag{3}$$

where $\boldsymbol{I} = \boldsymbol{E}_1 + \boldsymbol{E}_2 + \boldsymbol{E}_3$ is the 2nd order identity tensor ($\boldsymbol{E}_i := \boldsymbol{e}_i \otimes \boldsymbol{e}_i$ is the i:th base dyad), $\mathbf{I}^{sym} := \frac{1}{2}[\boldsymbol{I} \overline{\otimes} \boldsymbol{I} + \boldsymbol{I} \underline{\otimes} \boldsymbol{I}]$ is the (symmetric) 4th order

[1] It should be noted that the separator could simply be added to the model as an additional electrolyte domain. This would e.g. allow for other interface conditions linked to the convective flow at the electrode–separator interface.

[2] It is noted that $c_{Li}$ is defined in mol kg$^{-1}$, and not in mol m$^{-3}$ commonly used in the electro-chemistry literature (cf. Newman and Thomas-Alyea (2004)).

[3] That such a maximum value can be predefined follows from the explicit choice of the activity coefficient $f_{Li}(\tilde{c}_{Li})$.

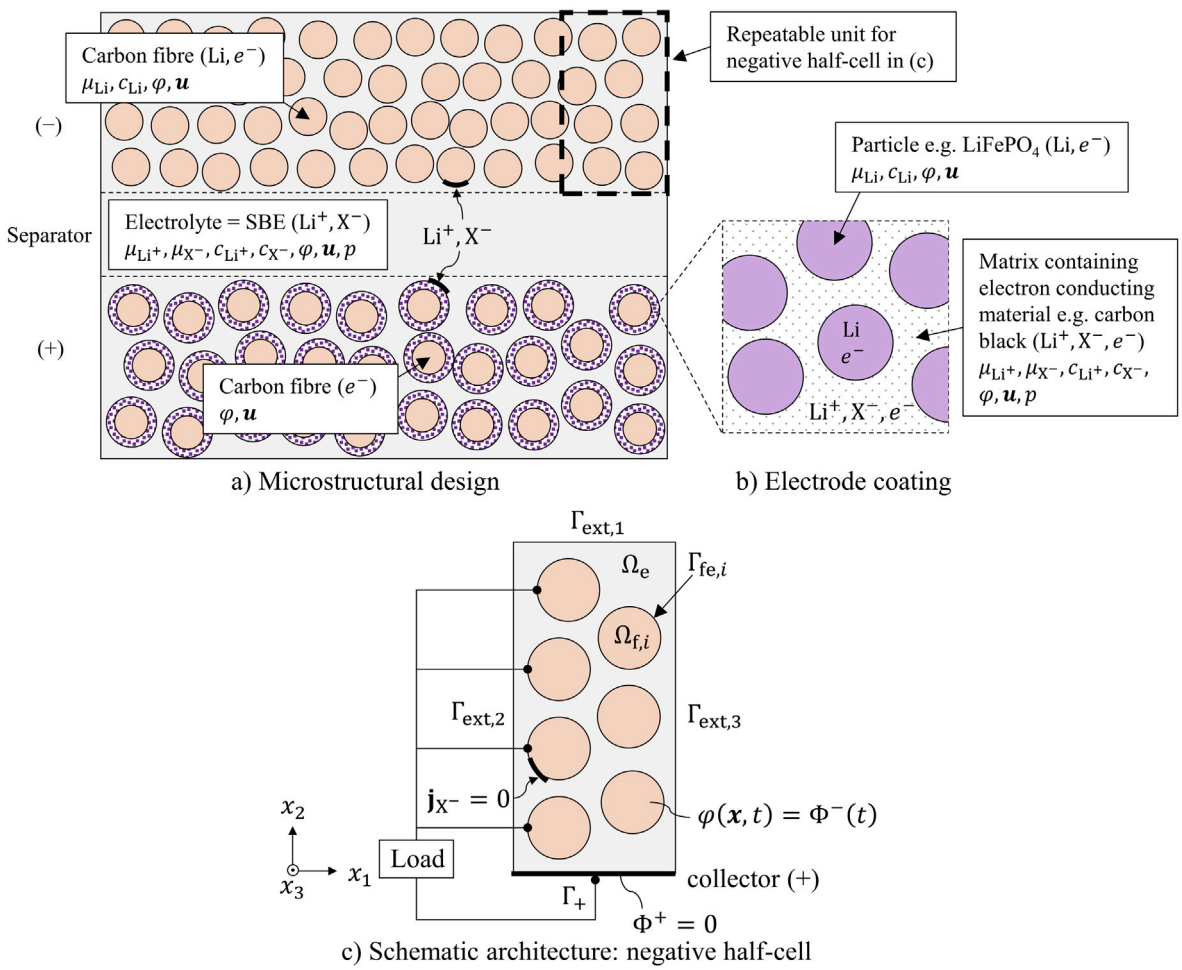


**Fig. 2.** (a) Possible (micro)structural design of the laminated structural battery comprising (−) and (+) electrodes with carbon fibres embedded in porous polymer electrolyte matrix (SBE). (b) Electrode coating with embedded Li-rich particles and matrix containing electron conductor (carbon black). (c) Schematic architecture (generic/idealized model representation) of the negative half-cell. In the external circuit, Load represents electric loading, e.g. in terms of a given resistance. The introduced notation is defined in Section 3.

identity tensor[4], whereas $\mathsf{A} := \frac{1}{4}[\boldsymbol{E}_3 \overline{\otimes} \boldsymbol{I} + \boldsymbol{E}_3 \underline{\otimes} \boldsymbol{I} + \boldsymbol{I} \overline{\otimes} \boldsymbol{E}_3 + \boldsymbol{I} \underline{\otimes} \boldsymbol{E}_3]$ is a 4th order symmetric tensor. Moreover, $L$ is Lamé's first parameter, $G$ is the shear modulus and $H_{\|}$ is the uniaxial strain modulus.

Next, the lithium insertion strain $\boldsymbol{\epsilon}^{\mathrm{ch}}(c_{\mathrm{Li}})$ and the mobility tensor $\boldsymbol{M}_{\mathrm{Li}}(c_{\mathrm{Li}})$ are introduced as follows:

$$\boldsymbol{\epsilon}^{\mathrm{ch}}(c_{\mathrm{Li}}) = \boldsymbol{\alpha}^{\mathrm{ch}} \left[c_{\mathrm{Li}} - c_{\mathrm{Li,ref}}\right], \text{ with } \boldsymbol{\alpha}^{\mathrm{ch}} = \alpha_{\perp}^{\mathrm{ch}} \left[\boldsymbol{E}_1 + \boldsymbol{E}_2\right] + \alpha_{\|}^{\mathrm{ch}} \boldsymbol{E}_3 \tag{4a}$$

$$\boldsymbol{M}_{\mathrm{Li}}(c_{\mathrm{Li}}) = M_{\mathrm{Li},\perp}(c_{\mathrm{Li}}) \left[\boldsymbol{E}_1 + \boldsymbol{E}_2\right] + M_{\mathrm{Li},\|}(c_{\mathrm{Li}}) \boldsymbol{E}_3 \tag{4b}$$

where the reference value $c_{\mathrm{Li,ref}}$ defines the state at which no chemical strains are present in the material. This value is set equal to 0 (for simplicity). The mobilities in the fibres in the transverse and longitudinal directions are denoted $M_{\mathrm{Li},\perp}(c_{\mathrm{Li}})$ and $M_{\mathrm{Li},\|}(c_{\mathrm{Li}})$, respectively.

### 3.2. Electrolyte domain $\Omega_e$

#### 3.2.1. Preliminaries

For the electrolyte domain we introduce the following special assumptions: (i) Material properties are characterized as isotropic. Hence, effective properties of the SBE are used (based on the properties of its two phases: liquid/solid); (ii) The Li-ions are positively charged (cation, $Li^+$), whereas the companion X-ions (anion, e.g. $PF_6^-$) are negatively charged; (iii) Convection in the pore fluid is accounted for as a transport mechanism for both the Li- and the X-ions; (iv) The current density is carried both by $Li^+$ and the companion anion $X^-$. There is no current due to motion of electrons, i.e. $\boldsymbol{i}_{e^-} = \boldsymbol{0}$; (v) The electric potential $\varphi$ may be discontinuous along each fibre–matrix interface $\Gamma_{\mathrm{fe},i}$, $i = 1, 2, \ldots, N_{\mathrm{fibres}}$. This discontinuity is modelled via a linearized Butler–Volmer type of "electric resistance" relation.

#### 3.2.2. Balance equations for SBE

The governing balance equations in the strong format are summarized as follows:

$$-\boldsymbol{\sigma} \cdot \boldsymbol{\nabla} = \boldsymbol{0} \text{ in } \Omega_e \times \mathbb{R}^+ \tag{5a}$$

$$\partial_t S + \hat{\boldsymbol{w}} \cdot \boldsymbol{\nabla} = 0 \text{ in } \Omega_e \times \mathbb{R}^+ \tag{5b}$$

$$-SF[c_{\mathrm{Li}} - c_{\mathrm{X}}] + \boldsymbol{d} \cdot \boldsymbol{\nabla} = 0 \text{ in } \Omega_e \times \mathbb{R}^+ \tag{5c}$$

$$\partial_t (S c_{\mathrm{Li}}) + \boldsymbol{j}_{\mathrm{Li}} \cdot \boldsymbol{\nabla} = 0 \text{ in } \Omega_e \times \mathbb{R}^+ \tag{5d}$$

$$\partial_t (S c_{\mathrm{X}}) + \boldsymbol{j}_{\mathrm{X}} \cdot \boldsymbol{\nabla} = 0 \text{ in } \Omega_e \times \mathbb{R}^+ \tag{5e}$$

where $S$ is the "fluid storage function" of liquid electrolyte salt and $\hat{\boldsymbol{w}}$ is the fluid mass flux. The balance Eqs. (5b), (5d) and (5e) represent novel developments in this context, cf. detailed derivation in Appendix A.[5]

[4] Indicial notation: $(\boldsymbol{A} \overline{\otimes} \boldsymbol{B})_{ijkl} \overset{\mathrm{def}}{=} (\boldsymbol{A})_{ik} (\boldsymbol{B})_{jl}$, $(\boldsymbol{A} \underline{\otimes} \boldsymbol{B})_{ijkl} \overset{\mathrm{def}}{=} (\boldsymbol{A})_{il} (\boldsymbol{B})_{jk}$ for $\boldsymbol{A}$, $\boldsymbol{B}$ symmetric 2nd order tensors.

[5] The equations are linearized around a reference porosity $\phi = \phi_0$ and a reference fluid density $\rho^{\mathrm{F}} = \rho_0^{\mathrm{F}}$, which both are considered as material constants. Further, Eqs. (5b), (5d) and (5e) correspond to Eqs. (A.15a) and (A.15b) in the Appendix A, where the ion fluxes $\boldsymbol{j}_\alpha$ for $\alpha$ = Li,X denotes the

Most importantly, the expressions are valid under the assumption of intrinsically compressible solid and fluid phases, whereby intrinsic incompressibility represents an extreme situation. Moreover, $\boldsymbol{d}$ is the electric flux density vector (dielectric displacement), $c_{\mathrm{Li}}$ and $c_{\mathrm{X}}$ are the ion concentrations, defined as ion mass (in moles) per unit mass of fluid (in kg), cf. Appendix B, and $F$ is Faraday's constant. For later use we also note that $\boldsymbol{i} = F[\boldsymbol{j}_{\mathrm{Li}} - \boldsymbol{j}_{\mathrm{X}}]$ is the current density due to motion of ions (known as Faraday's law of electrolysis).[6]

### 3.2.3. Constitutive relations for SBE

The relevant constitutive relations are:

$$\boldsymbol{\sigma} = \mathsf{E} : \boldsymbol{\epsilon}[\boldsymbol{u}] - \beta\, p\boldsymbol{I} \tag{6a}$$

$$S = \rho^{\mathrm{F}}\,[\phi + \lambda\, p + \beta[\boldsymbol{I} : \boldsymbol{\epsilon}[\boldsymbol{u}]]] \tag{6b}$$

$$\hat{\boldsymbol{w}} = -\boldsymbol{K} \cdot \boldsymbol{\nabla} p \tag{6c}$$

$$\boldsymbol{d} = -\boldsymbol{\mathcal{E}} \cdot \boldsymbol{\nabla}\varphi \tag{6d}$$

$$\boldsymbol{j}_{\mathrm{Li}} = -\boldsymbol{M}_{\mathrm{Li}} \cdot \boldsymbol{\nabla}\mu_{\mathrm{Li}} - F\boldsymbol{M}_{\mathrm{Li}} \cdot \boldsymbol{\nabla}\varphi + c_{\mathrm{Li}}\hat{\boldsymbol{w}} \tag{6e}$$

$$\text{where } \mu_{\mathrm{Li}} = \mu_{\mathrm{Li}}^{\mathrm{en}}(c_{\mathrm{Li}}) := \mu_{\mathrm{Li}}^{0} + R\theta_0 \log\left(\tilde{c}_{\mathrm{Li}}\right) \tag{6f}$$

$$\boldsymbol{j}_{\mathrm{X}} = -\boldsymbol{M}_{\mathrm{X}} \cdot \boldsymbol{\nabla}\mu_{\mathrm{X}} + F\boldsymbol{M}_{\mathrm{X}} \cdot \boldsymbol{\nabla}\varphi + c_{\mathrm{X}}\hat{\boldsymbol{w}} \tag{6g}$$

$$\text{where } \mu_{\mathrm{X}} = \mu_{\mathrm{X}}^{\mathrm{en}}(c_{\mathrm{X}}) := \mu_{\mathrm{X}}^{0} + R\theta_0 \log\left(\tilde{c}_{\mathrm{X}}\right) \tag{6h}$$

Eq. (6a) expresses the so-called "effective stress" principle of porous media; $\boldsymbol{\sigma}' = \mathsf{E} : \boldsymbol{\epsilon}[\boldsymbol{u}]$ is the effective stress, where $\mathsf{E} = L\boldsymbol{I} \otimes \boldsymbol{I} + 2G\mathbf{I}^{\mathrm{sym}}$ (expressed in terms of Lamé's parameters) is the standard isotropic elasticity tensor. Further, $p$ is the (intrinsic) pore pressure, and $\beta$ is the so-called Biot coefficient.

In (6b) we introduced the effective compressibility $\lambda$, whereas $\phi$ is the porosity of the SBE (in the undeformed state) and $\rho^{\mathrm{F}}$ is the intrinsic density of the fluid (electrolyte). How to obtain explicit values of $\beta$ and $\lambda$ is further elaborated in Appendix A. Indeed, the results used in this paper are given in (A.22a) and (A.22b).

The isotropic permeability (hydraulic conductivity) tensor $\boldsymbol{K}$, introduced in (6c), is defined as $\boldsymbol{K} := \rho^{\mathrm{F}} k\boldsymbol{I}$, where $k$ is the permeability coefficient.

The isotropic permittivity tensor $\boldsymbol{\mathcal{E}}$, introduced in (6d), is defined as $\boldsymbol{\mathcal{E}} := \varepsilon\boldsymbol{I}$, where $\varepsilon = \varepsilon_0\varepsilon_r$ is the permittivity (i.e. the material's ability to transmit an electric field). The permittivity in vacuum, is denoted $\varepsilon_0$, and the relative permittivity is denoted $\varepsilon_r$. The electrical potential is $\varphi$.

The isotropic mobility tensors, introduced in (6e) and (6g), are defined as $\boldsymbol{M}_{\mathrm{Li}}(c_{\mathrm{Li}}) = \eta_{\mathrm{Li}}\rho^{\mathrm{F}}c_{\mathrm{Li}}\boldsymbol{I}$ and $\boldsymbol{M}_{\mathrm{X}}(c_{\mathrm{X}}) = \eta_{\mathrm{X}}\rho^{\mathrm{F}}c_{\mathrm{X}}\boldsymbol{I}$, where $\eta_\alpha$ is the mobility coefficient of species $\alpha$ for $\alpha = \mathrm{Li,X}$. It should be noted that we have made the simplification that there is no coupling between the diffusion of $\mathrm{Li}^+$ and $\mathrm{X}^-$. Upon comparing with (A.16), we note that the first two terms in (6e) and (6g) are associated with diffusion and migration, ($\boldsymbol{j}_\alpha^{\mathrm{D}}$), while the last term corresponds to the convective contribution of the ion flux, ($\boldsymbol{j}_\alpha^{\mathrm{C}}$). As to the chemical potentials $\mu_{\mathrm{Li}}$ and $\mu_{\mathrm{X}}$, which are defined in (6f) and (6h), respectively, we define the normalized ion concentration of species Li and X in the electrolyte as $\tilde{c}_{\mathrm{Li}} = \frac{c_{\mathrm{Li}}}{c_{\mathrm{Li,ref}}}$ and $\tilde{c}_{\mathrm{X}} = \frac{c_{\mathrm{X}}}{c_{\mathrm{X,ref}}}$, respectively. Both $c_{\mathrm{Li,ref}}$ and $c_{\mathrm{X,ref}}$ are chosen as 1 mol kg$^{-1}$.[7] It should be noted that the chemical potential for the species in the electrolyte (Eqs. (6f) and (6h)) are defined in accordance with the standard definition for an ideal solution (see e.g. Chapter 2 in Newman and Thomas-Alyea (2004)). This can be compared with the definition for $\mu_{\mathrm{Li}}$ in the fibre (Eq. (2c)) which is modified to account for the phase separation occurring during intercalation (i.e. modelled as a lattice gas or an ideal mixture of particles and holes, see Bazant, 2014) and the effect of mechanical stress (cf. Larché and Cahn, 1985).

combined motion from diffusion, migration and convection (i.e. the sum of $\boldsymbol{j}_\alpha^{\mathrm{D}}$ and $\boldsymbol{j}_\alpha^{\mathrm{C}}$).

[6] Here, we used that the valence number is +1 for Li and −1 for X.

[7] This value is obtained from setting $\rho^{\mathrm{F}}c_{\alpha,\mathrm{ref}} = 1$ molar (or $10^3$ mol m$^{-3}$) and $\rho^{\mathrm{F}} = 10^3$ kg m$^{-3}$.

Finally, upon combining the expressions above, we derive the constitutive relation for the current density:

$$\boldsymbol{i} = -F\boldsymbol{M}_{\mathrm{Li}} \cdot \boldsymbol{\nabla}\mu_{\mathrm{Li}} + F\boldsymbol{M}_{\mathrm{X}} \cdot \boldsymbol{\nabla}\mu_{\mathrm{X}} - \boldsymbol{\mathcal{K}} \cdot \boldsymbol{\nabla}\varphi - \boldsymbol{C} \cdot \boldsymbol{\nabla} p \tag{7}$$

where we introduced the ionic conductivity $\boldsymbol{\mathcal{K}} := F^2[\boldsymbol{M}_{\mathrm{Li}} + \boldsymbol{M}_{\mathrm{X}}]$ and the ionic permeability $\boldsymbol{C} := F[c_{\mathrm{Li}} - c_{\mathrm{X}}]\boldsymbol{K}$.

**Remark 1.** A common assumption in the electro-chemistry literature on conventional Li-ion batteries is electroneutrality, i.e. $F[c_{\mathrm{Li}} - c_{\mathrm{X}}] = 0$ cf. Newman and Thomas-Alyea (2004)). When this condition is fulfilled, (i) Gauss law in Eq. (5c) becomes homogeneous and (ii) the convective contribution to the current density in Eq. (7) disappears ($\boldsymbol{C} = \boldsymbol{0}$). It should be noted that noticeable deviation from electroneutrality only occurs in the immediate vicinity of electrode–electrolyte interfaces (see e.g. Carlstedt et al. (2020)) and that proposed framework does not require this condition to be fulfilled. □

### 3.2.4. Material properties of SBE - Dependence on porosity

The porosity of the SBE, $\phi$, depends significantly on the composition of the polymer/electrolyte mixture (e.g. different monomers or mixing ratios of monomer to electrolyte before curing) (Ihrner et al., 2017; Schneider et al., 2019). Clearly, the effective properties, such as elastic stiffness $\mathsf{E}$, permeability $\boldsymbol{K}$ and mobilities $\boldsymbol{M}_{\mathrm{Li}}, \boldsymbol{M}_{\mathrm{X}}$, depend strongly on $\phi$. Due to the fact that the SBE consists of two phases (liquid/solid) and that the porosity/phase separation exists at the nano-scale (compare with the micro-scale of the utilized model), effective properties of the SBE (micro-scale) can be derived via virtual material testing on (nano-scale) Representative Volume Elements (RVEs).

In this paper we exploit results obtained by Tu et al. (2020). Artificial RVEs are generated to mimic the geometry of the SBE, see Fig. 3.

These artificially generated RVEs are then used to characterize the effective (microscopic) properties via computational homogenization. The elastic bulk modulus $B$ and shear modulus $G$ are computed based on assumed isotropic linear elasticity on the sub-scale. The effective mobility $\eta_\alpha$ of species $\alpha$ in the SBE is computed by solving the diffusion equation in the pore domain of the RVE. Finally, the permeability $k$ is identified by solving the Stokes flow problem in the pore domain, while assuming a rigid skeleton. The homogenized effective properties are extracted from RVEs with different porosity values in the range $0.2 < \phi < 0.8$. This range was used since bicontinuity of the porous microstructure might be lost in the intervals $0 < \phi < 0.2$ and $0.8 < \phi < 1$. Moreover, setting the RVE size to 500 nm results in a characteristic pore size of roughly 100 nm, which is in accordance with Ihrner et al. (2017), Schneider et al. (2019). Since the considered RVEs are not sufficiently large to be fully representative, we compute quasi-isotropic effective properties by averaging the approximately isotropic components into one single value in the same fashion as in the paper by Tu et al. (2020). By using this averaging method, they show that the resulting variations of the effective properties between randomly generated RVEs within the same microstructure class are small. Further, it should be noted that the results that are derived from using this method are only valid for the microstructure class pertaining to bicontinuous RVE microstructures, i.e. two-phase systems with intermingling solid and liquid phases as observed in structural battery electrolytes (Ihrner et al., 2017; Schneider et al., 2019).

In order to extract the effective properties as smooth functions of $\phi$, we employ various interpolation laws based on the discrete data points that represent the RVE-computations. The generalized mixture rule, which defines a generic property $\chi$, can be formulated as

$$\chi = \left[\phi a_1^b + [1-\phi]\, a_2^b\right]^{1/b}, \quad b \in [-1, 1]\backslash\{0\} \tag{8}$$

where the exponent $b$ allows for an interpolation between the arithmetic mean $b = 1$ and the harmonic mean $b = -1$. The constants $a_1$ and $a_2$ prescribe the interpolation curve at $\phi = 1$ and $\phi = 0$ respectively. For the mechanical properties, such as the bulk modulus and the shear modulus, we set $a_1 = 0$ (liquid phase in pore space) whereby $a_2$ will

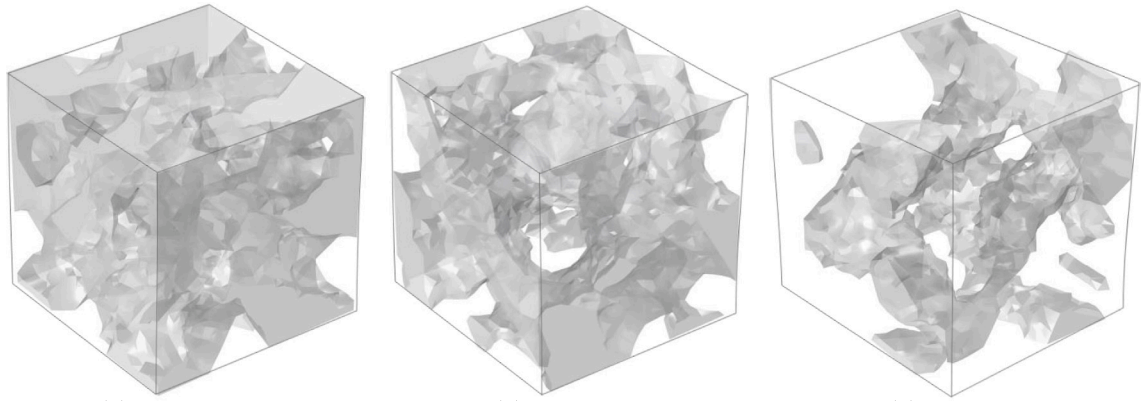


**Fig. 3.** Example RVE samples representing the nano-scale SBE of various porosities ($\phi$). The grey body represents the solid polymer phase of the SBE, while the empty space is filled with liquid electrolyte.

represent the intrinsic bulk modulus $B^{\mathrm{S}}$ and shear modulus $G^{\mathrm{S}}$ of the solid phase, respectively. The interpolation rule for the bulk modulus and the shear modulus thus simplifies to

$$B = [1-\phi]^{1/b}\, B^{\mathrm{S}},\ b \in [-1,1]\backslash\{0\} \tag{9}$$

$$G = [1-\phi]^{1/b}\, G^{\mathrm{S}},\ b \in [-1,1]\backslash\{0\} \tag{10}$$

where the exponent $b$ corresponds to the only free parameter which is determined via curve fitting.

The same arguments are applied for representation of the ionic mobility. Hence, $a_1$ is set equal to the intrinsic ionic mobility $\eta^{\mathrm{F}}$ (liquid phase in the pore space), whereas $a_2 = 0$ in the electro-chemically inactive solid phase. This means that the SBE would lose all of its mobility in the event of a dense material, $\phi = 0$. Clearly, it would perform as a purely liquid electrolyte in the extreme situation that $\phi = 1$. The interpolation rule for the ionic mobility thus reduces to

$$\eta = \phi^{1/b}\eta^{\mathrm{F}},\ b \in [-1,1]\backslash\{0\} \tag{11}$$

which corresponds to the Bruggeman relation if we identify $1/b$ as the Bruggeman exponent (Newman and Tiedemann, 1975; Bruggeman, 1937).

Finally, for the effective permeability, we adopt the Kozeny–Carman rule (Carman, 1997) which is used for predicting the permeability in porous media

$$k = a_3 \frac{\phi^3}{[1-\phi]^2} \tag{12}$$

where the proportionality constant $a_3$ corresponds to the only free parameter which is determined via curve fitting. It should be noted that the Kozeny–Carman rule is commonly used in the electro-chemistry literature for estimating the permeability of porous electrodes in flow batteries, see e.g. Xu and Zhao (2015) and Esan et al. (2020).

### 3.3. The fibre/electrolyte interface $\Gamma_{fe}$

We assume that the redox reactions and load transfer occur along the entire fibre–electrolyte interface with uniform properties. The fibre–electrolyte interfaces are assumed to be perfectly bonded such that the displacement field $\boldsymbol{u}$ is continuous across $\Gamma_{\mathrm{fe}}$. Further, we assume that $\mu_{\mathrm{Li}}$, as well as $\varphi$, may be discontinuous across $\Gamma_{\mathrm{fe}}$, whereas $j_{\mathrm{Li},n}$ is continuous across $\Gamma_{\mathrm{fe}}$. Finally, we note that no seepage takes place across the interface, i.e. $\hat{w}_n := \hat{\boldsymbol{w}} \cdot \boldsymbol{n} = 0$ on $\Gamma_{\mathrm{fe}}$, where $\boldsymbol{n}$ is the normal on $\Gamma_{\mathrm{fe}}$ pointing out from the electrolyte domain $\Omega_{\mathrm{e}}$ and into the fibre domain $\Omega_{\mathrm{f}}$.

We assume that $j_{\mathrm{Li},n}$ is governed constitutively by an interface mobility $\bar{M}$ such that

$$\begin{aligned} j_{\mathrm{Li},n}(\boldsymbol{x}) &:= \boldsymbol{j}_{\mathrm{Li}}(\boldsymbol{x}) \cdot \boldsymbol{n}(\boldsymbol{x}) \\ &= -\bar{M}[\![\mu'_{\mathrm{Li}}]\!](\boldsymbol{x}) = -\bar{M}[\![\mu_{\mathrm{Li}}]\!](\boldsymbol{x}) - F\bar{M}\left[\Phi^- - \varphi^{\mathrm{e}}\right],\ \boldsymbol{x} \in \Gamma_{\mathrm{fe}} \end{aligned} \tag{13}$$

In Eq. (13), we introduced the jump operator $[\![\bullet]\!](\boldsymbol{x}) := \bullet(\boldsymbol{x}^{\mathrm{f}}) - \bullet(\boldsymbol{x}^{\mathrm{e}})$ and $\boldsymbol{x}^{\mathrm{f}} := \lim_{\epsilon\downarrow 0}[\boldsymbol{x} + \epsilon\boldsymbol{n}]$, $\boldsymbol{x}^{\mathrm{e}} := \lim_{\epsilon\downarrow 0}[\boldsymbol{x} - \epsilon\boldsymbol{n}]$. Further, we used the identity $[\![\mu'_{\mathrm{Li}}]\!] = [\![\mu_{\mathrm{Li}}]\!] + F\left[\Phi^- - \varphi^{\mathrm{e}}\right]$, where $\varphi^{\mathrm{e}} := \varphi(\boldsymbol{x}^{\mathrm{e}})$ is evaluated in the electrolyte at the fibre–electrolyte interface. Clearly, this model carries over directly to the current density flux $i_n$ across the interface $\Gamma_{\mathrm{fe}}$, i.e.

$$\begin{aligned} i_n &= F[j_{\mathrm{Li},n} - \underbrace{j_{\mathrm{X},n}}_{=0}] = -F\bar{M}[\![\mu_{\mathrm{Li}}]\!] - \bar{\mathcal{K}}\left[\Phi^- - \varphi^{\mathrm{e}}\right] \\ &= -F\bar{M}[\mu^{\mathrm{f}}_{\mathrm{Li}} - \mu^{\mathrm{e}}_{\mathrm{Li}}] - \bar{\mathcal{K}}\left[\Phi^- - \varphi^{\mathrm{e}}\right] \ \text{ on } \Gamma_{\mathrm{fe}} \end{aligned} \tag{14}$$

where we introduced the assumption $j_{\mathrm{X},n}(\boldsymbol{x}^{\mathrm{e}}) = 0,\ \boldsymbol{x} \in \Gamma_{\mathrm{fe}}$, i.e. the transport of $\mathrm{X}^-$ is blocked at the fibre–electrolyte interface. The chemical potential in the fibre and electrolyte is denoted $\mu^{\mathrm{f}}_{\mathrm{Li}}$ and $\mu^{\mathrm{e}}_{\mathrm{Li}}$, respectively, and the interface ionic conductivity is introduced as $\bar{\mathcal{K}} := F^2\bar{M}$. Further, we introduce the constitutive assumption

$$d_n = -\bar{\mathcal{E}}\left[\Phi^- - \varphi^{\mathrm{e}}\right] \ \text{ on } \Gamma_{\mathrm{fe}} \tag{15}$$

where $d_n$ is the electric flux density vector and $\bar{\mathcal{E}}$ is the interface permittivity.

**Remark 2.** The relation (14) is identical to a linearized Butler–Volmer relation, see e.g. Newman and Thomas-Alyea (2004). □

Finally, we note that the current $I^-(t)$ corresponds to the total current in all the fibres that are connected to the negative connector. This current has to be transported/conducted via electronic conduction along the fibres; however, it cannot be modelled in a 2D-setting. Its value is known (prescribed) in the case of a galvanostatic problem, whereas it is a "reaction" in the case of a potentiostatic problem.

### 3.4. Exterior boundaries $\Gamma_{ext} \cup \Gamma_+$

Mechanical conditions are related to displacements ($\boldsymbol{u}$) and tractions ($\boldsymbol{\sigma}_n = \boldsymbol{\sigma} \cdot \boldsymbol{n}$):

$$u_1 = \bar{u}_1,\ \sigma_{n,2} = 0 \text{ on } \Gamma_{\mathrm{ext},2} \cup \Gamma_{\mathrm{ext},3} \tag{16a}$$

$$\boldsymbol{\sigma}_n = \boldsymbol{0} \text{ on } \Gamma_{\mathrm{ext},1} \cup \Gamma_+ \tag{16b}$$

where $\bar{u}_1$ denotes time-dependent prescribed displacement (to be parameterized later). Further, mechanical conditions related to pore pressure ($p$) and seepage ($\hat{w}_n = \hat{\boldsymbol{w}} \cdot \boldsymbol{n}$) are defined as:

$$p = 0 \text{ on } \Gamma_{\mathrm{ext},1} \tag{17a}$$

$$\hat{w}_n = 0 \text{ on } \Gamma_{\text{ext},2} \cup \Gamma_{\text{ext},3} \cup \Gamma_+ \tag{17b}$$

The motivation for the traction-free condition on $\Gamma_{\text{ext},1} \cup \Gamma_+$ in Eq. (16b) is that the studied (part of the) lamina will in practice constitute a layered plate structure, whereby the assumption about small magnitude of the normal stress across the plate thickness is well taken. Moreover, the liquid phase in the SBE is allowed to flow freely through the upper boundary of the unit cell $\Gamma_{\text{ext},1}$ (i.e. permeable surface), as the pore pressure is set to zero (cf. Eq. (17a)). This boundary condition is motivated for the structural battery design used in previous experimental studies, e.g. Asp et al. (2021) and Johannisson et al. (2018). In these studies, the upper surface of the carbon fibre electrode was freely exposed towards the inside of a pouch cell bag. It should be noted that under these conditions, the liquid electrolyte content within the unit cell is allowed to vary.

Chemical conditions are related to ion flux ($j_{\text{Li},n} = \boldsymbol{j}_{\text{Li}} \cdot \boldsymbol{n}$, $j_{\text{X},n} = \boldsymbol{j}_{\text{X}} \cdot \boldsymbol{n}$):

$$j_{\text{Li},n} = -F\bar{M}\left[\Phi^+ - \varphi^{\text{e}}\right] \text{ on } \Gamma_+ \tag{18a}$$

$$j_{\text{Li},n} = 0 \text{ on } \Gamma_{\text{ext},2} \cup \Gamma_{\text{ext},3} \tag{18b}$$

$$j_{Li,n} = c_{\text{Li}} \hat{w}_n \text{ on } \Gamma_{\text{ext},1} \tag{18c}$$

$$j_{X,n} = 0 \text{ on } \Gamma_{\text{ext},2} \cup \Gamma_{\text{ext},3} \cup \Gamma_+ \tag{18d}$$

$$j_{X,n} = c_{\text{X}} \hat{w}_n \text{ on } \Gamma_{\text{ext},1} \tag{18e}$$

The assumed chemical conditions are motivated by the fact that the ion flux occurs between the Li-metal and fibres (i.e. mainly in the $x_2$-direction in Fig. 2c) and that the height of the studied unit corresponds to the thickness of the electrode lamina. Moreover, in accordance with the assumption of permeable upper surface $\Gamma_{\text{ext},1}$ (cf. Eq. (17a)), a convective contribution (driven by the pressure gradient) of the ion flux is allowed along this surface.

Electrical conditions are related to the electric flux density ($d_n$):

$$d_n = -\bar{\mathcal{E}}\left[\Phi^+ - \varphi^{\text{e}}\right] \text{ on } \Gamma_+ \tag{19a}$$

$$d_n = 0 \text{ on } \Gamma_{\text{ext}} \tag{19b}$$

where $\Gamma_{\text{ext}}$ denotes all exterior boundaries except $\Gamma_+$. Further, $\Phi^+$ is a spatially constant value in the collector (Li-metal) at $\Gamma_+$ and $\varphi^{\text{e}}$ is the electrolyte potential along $\Gamma_+$. Moreover, we assume that $\Phi^+$ is henceforth prescribed at 0 V (as a given reference potential).

### 3.5. Convention for discharging and (re)charging phases

For charge/discharge conditions we utilize the convention of a carbon fibre electrode vs. Li-metal half-cell (cf. Carlstedt et al., 2020). The distinct phases of discharging and charging are summarized as follows:

**Charging (delithiation)**: The electric loading device is disconnected and either a potentiostatic or galvanostatic problem is solved. During charging the fibres are delithiated, i.e. Li-ions move from the fibres to the Li-metal. This phase ends when the battery is fully charged, i.e. when either $\Phi^-(t)$ or $I^-(t)$ reaches a predefined threshold value.

**Discharging (lithiation)**: The electric loading device is connected. During discharging the fibres are lithiated, i.e. Li-ions move from the Li-metal to the fibres. This phase ends when either $\Phi^-(t)$ or $I^-(t)$ falls below a predefined threshold value.

## 4. Time-incremental weak format of half-cell problem

### 4.1. Preliminaries

We introduce time intervals $I_n = (t_{n-1}, t_n)$, whose length is $\Delta t = t_n - t_{n-1}$. We then employ the Backward Euler method for time integration; however, we deviate from the fully implicit rule by replacing the constitutive mobility tensor $\boldsymbol{M}_\alpha({}^n c_\alpha)$ by ${}^{n-1}\boldsymbol{M}_\alpha := \boldsymbol{M}_\alpha({}^{n-1}c_\alpha)$ for $\alpha =$ Li,X, which infers forward differencing. Hence, we evaluate $\boldsymbol{j}_\alpha := {}^n\boldsymbol{j}_\alpha$ at $t = t_n$ as

$$\boldsymbol{j}_\alpha(\nabla\mu_\alpha, \nabla\varphi, \nabla p) = -{}^{n-1}\boldsymbol{M}_\alpha \cdot \nabla\mu_\alpha - {}^{n-1}\boldsymbol{\mathcal{L}}_\alpha \cdot \nabla\varphi - {}^{n-1}c_\alpha \boldsymbol{K} \cdot \nabla p, \ \alpha = \text{Li,X} \tag{20}$$

where $\boldsymbol{\mathcal{L}}_{\text{Li}} = F\boldsymbol{M}_{\text{Li}}$ and $\boldsymbol{\mathcal{L}}_{\text{X}} = -F\boldsymbol{M}_{\text{X}}$.

The relevant solution (and test) spaces for solutions at the updated time $t_n$ are defined as:

$$\hat{\mathbb{U}} = \{\boldsymbol{u} \in \mathbb{H}^1(\Omega) : \ u_1 = \bar{u}_1 \text{ on } \Gamma_{\text{ext},2} \cup \Gamma_{\text{ext},3}, \}$$

$$\hat{\mathbb{U}}^0 = \{\boldsymbol{u} \in \mathbb{H}^1(\Omega) : \ u_1 = 0 \text{ on } \Gamma_{\text{ext},2} \cup \Gamma_{\text{ext},3}\} \tag{21a}$$

$$\hat{\mathbb{P}} = \hat{\mathbb{P}}^0 = \{p \in \mathbb{H}^1(\Omega_{\text{e}}) : \ p = 0 \text{ on } \Gamma_{\text{ext},1}\} \tag{21b}$$

$$\hat{\mathbb{F}} = \hat{\mathbb{F}}^0 = \{\varphi \in \mathbb{H}^1(\Omega_{\text{e}})\} \tag{21c}$$

$$\hat{\mathbb{M}}_{\text{Li}} = \hat{\mathbb{M}}^0_{\text{Li}} = \{\mu_{\text{Li}} \in \mathbb{L}_2(\Omega_{\text{f}} \cup \Omega_{\text{e}}), \ \mu_{\text{Li}}|_{\Omega_{\text{f}}} = \mathbb{H}^1(\Omega_{\text{f}}), \ \mu_{\text{Li}}|_{\Omega_{\text{e}}} = \mathbb{H}^1(\Omega_{\text{e}})\} \tag{21d}$$

$$\hat{\mathbb{M}}_{\text{X}} = \hat{\mathbb{M}}^0_{\text{X}} = \{\mu_{\text{X}} \in \mathbb{H}^1(\Omega_{\text{e}})\} \tag{21e}$$

### 4.2. Potentiostatic problem – Controlling the electric potential $\Phi^-(t)$

The potential value $\Phi^-(t)$ (in addition to $\Phi^+(t) = 0$) is a prescribed function in time within the negative collector (fibre) domains $\Omega_{\text{f}} := \cup_i \Omega_{\text{f},i}$. The entire problem of solving for the updated fields at $t = t_n$ can now be posed as follows: Find $\boldsymbol{u} \in \hat{\mathbb{U}}$, $p \in \hat{\mathbb{P}}$, $\varphi \in \hat{\mathbb{F}}$, $\mu_{\text{Li}} \in \hat{\mathbb{M}}_{\text{Li}}$, $\mu_{\text{X}} \in \hat{\mathbb{M}}_{\text{X}}$, $c_{\text{Li}} \in \mathbb{L}_2(\Omega_{\text{f}} \cup \Omega_{\text{e}})$, and $c_{\text{X}} \in \mathbb{L}_2(\Omega_{\text{e}})$, that solve the set of equations

$$\int_{\Omega_{\text{f}} \cup \Omega_{\text{e}}} \boldsymbol{\sigma} : \epsilon[\delta\boldsymbol{u}] \, \text{d}V = 0 \qquad \forall \delta\boldsymbol{u} \in \hat{\mathbb{U}}^0 \tag{22a}$$

$$-\frac{1}{\Delta t}\int_{\Omega_{\text{e}}} \left[S - {}^{n-1}S\right] \delta p \, \text{d}V + \int_{\Omega_{\text{e}}} \hat{\boldsymbol{w}} \cdot \nabla[\delta p] \, \text{d}V = 0 \qquad \forall \delta p \in \hat{\mathbb{P}}^0 \tag{22b}$$

$$\int_{\Omega_{\text{e}}} SF\left[c_{\text{Li}} - c_{\text{X}}\right] \delta\varphi \, \text{d}V + \int_{\Omega_{\text{e}}} \boldsymbol{d} \cdot \nabla[\delta\varphi] \, \text{d}V - \int_{\Gamma_{\text{fe}} \cup \Gamma_+} d_n \delta\varphi \, \text{d}S = 0 \qquad \forall \delta\varphi \in \hat{\mathbb{F}}^0 \tag{22c}$$

$$\begin{aligned} &-\frac{1}{\Delta t}\int_{\Omega_{\text{f}}} \rho\left[c_{\text{Li}} - {}^{n-1}c_{\text{Li}}\right] \delta\mu_{\text{Li}} \, \text{d}V \\ &-\frac{1}{\Delta t}\int_{\Omega_{\text{e}}} \left[Sc_{\text{Li}} - {}^{n-1}[Sc_{\text{Li}}]\right] \delta\mu_{\text{Li}} \, \text{d}V \\ &+\int_{\Omega_{\text{f}} \cup \Omega_{\text{e}}} \boldsymbol{j}_{\text{Li}} \cdot \nabla[\delta\mu_{\text{Li}}] \, \text{d}V + \int_{\Gamma_{\text{fe}}} j_{\text{Li},n} [\![\delta\mu_{\text{Li}}]\!] \, \text{d}S \\ &-\int_{\Gamma_+ \cup \Gamma_{\text{ext},1}} j_{\text{Li},n} \, \delta\mu_{\text{Li}} \, \text{d}S = 0 \qquad \forall \delta\mu_{\text{Li}} \in \hat{\mathbb{M}}^0_{\text{Li}} \end{aligned} \tag{22d}$$

$$\begin{aligned} &-\frac{1}{\Delta t}\int_{\Omega_{\text{e}}} \left[Sc_{\text{X}} - {}^{n-1}[Sc_{\text{X}}]\right] \delta\mu_{\text{X}} \, \text{d}V \\ &+\int_{\Omega_{\text{e}}} \boldsymbol{j}_{\text{X}} \cdot \nabla[\delta\mu_{\text{X}}] \, \text{d}V - \int_{\Gamma_{\text{ext},1}} j_{\text{X},n} \, \delta\mu_{\text{X}} \, \text{d}S = 0 \qquad \forall \delta\mu_{\text{X}} \in \hat{\mathbb{M}}^0_{\text{X}} \end{aligned} \tag{22e}$$

$$\int_{\Omega_{\text{f}} \cup \Omega_{\text{e}}} \left[\mu^{\text{en}}_{\text{Li}} - \mu_{\text{Li}}\right] \delta c_{\text{Li}} \, \text{d}V = 0 \qquad \forall \delta c_{\text{Li}} \in \mathbb{L}_2(\Omega_{\text{f}} \cup \Omega_{\text{e}}) \tag{22f}$$

$$\int_{\Omega_{\text{e}}} \left[\mu^{\text{en}}_{\text{X}} - \mu_{\text{X}}\right] \delta c_{\text{X}} \, \text{d}V = 0 \qquad \forall \delta c_{\text{X}} \in \mathbb{L}_2(\Omega_{\text{e}}) \tag{22g}$$

where the pertinent constitutive relations were given as follows: $\boldsymbol{\sigma}$ is defined in Eq. (2a) on $\Omega_{\text{f}}$ and in Eq. (6a) on $\Omega_{\text{e}}$; $\boldsymbol{d}$ is defined in Eq. (6d) on $\Omega_{\text{e}}$; $\boldsymbol{j}_{\text{Li}}$ is defined in Eq. (2b) on $\Omega_{\text{f}}$ and in Eq. (6e) on $\Omega_{\text{e}}$; $\boldsymbol{j}_{\text{X}}$ is defined in Eq. (6g) on $\Omega_{\text{e}}$; $\hat{\boldsymbol{w}}$ is defined in Eq. (6c) on $\Omega_{\text{e}}$; $\mu^{\text{en}}_{\text{Li}}$ and $\mu^{\text{en}}_{\text{X}}$ are the energetic constitutive expressions of Eqs. (2c), (6f) and (6h). Moreover, $j_{\text{Li},n}$ is defined in Eq. (13) on $\Gamma_{\text{fe}}$, in Eq. (18a) on $\Gamma_+$ and in Eq. (18c) on $\Gamma_{\text{ext},1}$. In addition, $j_{\text{X},n}$ is defined in Eq. (18e) on $\Gamma_{\text{ext},1}$. Finally, $d_n$ is defined in Eq. (15) on $\Gamma_{\text{fe}}$ and in (19a) on $\Gamma_+$.

**Remark 3.** We employ a mixed method, since $\mu_{\text{Li}}$ and $\mu_{\text{X}}$ are treated as independent fields in addition to $c_{\text{Li}}$ and $c_{\text{X}}$. This choice requires the additional constraint conditions in Eqs. (22f) and (22g). □

The current $I^-$ is computed in a postprocessing step as

$$I^- = \int_{\Gamma_{\text{fe}}} i_n \, \text{d}S \tag{23}$$

where the constitutive relation for $i_n$ was given in Eq. (14).

### 4.3. Galvanostatic problem – Controlling the electric current $I^-(t)$

The potential value $\Phi^+(t)$ is prescribed along the boundary $\Gamma_+$, whereas the total current $I^-(t)$ from/to the negative collector (fibre) domains $\Omega_f := \cup_i \Omega_{f,i}$ is assumed to be a known function. The entire problem of solving for the updated fields at $t = t_n$ can now be posed as follows: Find $\boldsymbol{u} \in \hat{\mathbb{U}}$, $p \in \hat{\mathbb{P}}$, $\varphi \in \hat{\mathbb{F}}$, $\mu_{Li} \in \hat{\mathbb{M}}_{Li}$, $\mu_X \in \hat{\mathbb{M}}_X$, $c_{Li} \in \mathbb{L}_2(\Omega_f \cup \Omega_e)$, $c_X \in \mathbb{L}_2(\Omega_e)$, and $\Phi^- \in \mathbb{R}$, that solve the set of equations

$$\int_{\Omega_i \cup \Omega_e} \boldsymbol{\sigma} : \epsilon[\delta \boldsymbol{u}] \, \mathrm{d}V = 0 \qquad \forall \delta \boldsymbol{u} \in \hat{\mathbb{U}}^0 \tag{24a}$$

$$-\frac{1}{\Delta t} \int_{\Omega_e} \left[S - {}^{n-1}S\right] \delta p \, \mathrm{d}V + \int_{\Omega_e} \hat{\boldsymbol{u}} \cdot \nabla[\delta p] \, \mathrm{d}V = 0 \qquad \forall \delta p \in \hat{\mathbb{P}}^0 \tag{24b}$$

$$\int_{\Omega_e} SF\left[c_{Li} - c_X\right] \delta\varphi \, \mathrm{d}V + \int_{\Omega_e} \boldsymbol{d} \cdot \nabla[\delta\varphi] \, \mathrm{d}V - \int_{\Gamma_{fe} \cup \Gamma_+} d_n \delta\varphi \, \mathrm{d}S = 0 \qquad \forall \delta\varphi \in \hat{\mathbb{F}}^0 \tag{24c}$$

$$\begin{aligned} &-\frac{1}{\Delta t} \int_{\Omega_f} \rho \left[c_{Li} - {}^{n-1}c_{Li}\right] \delta\mu_{Li} \, \mathrm{d}V \\ &-\frac{1}{\Delta t} \int_{\Omega_e} \left[Sc_{Li} - {}^{n-1}[Sc_{Li}]\right] \delta\mu_{Li} \, \mathrm{d}V \\ &+ \int_{\Omega_f \cup \Omega_e} \boldsymbol{j}_{Li} \cdot \nabla[\delta\mu_{Li}] \, \mathrm{d}V + \int_{\Gamma_{fe}} j_{Li,n} [\![\delta\mu_{Li}]\!] \, \mathrm{d}S \\ &- \int_{\Gamma_+ \cup \Gamma_{ext,1}} j_{Li,n} \delta\mu_{Li} \, \mathrm{d}S = 0 \qquad \forall \delta\mu_{Li} \in \hat{\mathbb{M}}^0_{Li} \end{aligned} \tag{24d}$$

$$\begin{aligned} &-\frac{1}{\Delta t} \int_{\Omega_e} \left[Sc_X - {}^{n-1}[Sc_X]\right] \delta\mu_X \, \mathrm{d}V \\ &+ \int_{\Omega_e} \boldsymbol{j}_X \cdot \nabla[\delta\mu_X] \, \mathrm{d}V - \int_{\Gamma_{ext,1}} j_{X,n} \delta\mu_X \, \mathrm{d}S = 0 \qquad \forall \delta\mu_X \in \hat{\mathbb{M}}^0_X \end{aligned} \tag{24e}$$

$$\int_{\Omega_i \cup \Omega_e} \left[\mu^{en}_{Li} - \mu_{Li}\right] \delta c_{Li} \, \mathrm{d}V = 0 \qquad \forall \delta c_{Li} \in \mathbb{L}_2(\Omega_f \cup \Omega_e) \tag{24f}$$

$$\int_{\Omega_e} \left[\mu^{en}_X - \mu_X\right] \delta c_X \, \mathrm{d}V = 0 \qquad \forall \delta c_X \in \mathbb{L}_2(\Omega_e) \tag{24g}$$

$$\delta\Phi^- \left[\int_{\Gamma_{fe}} i_n \, \mathrm{d}S - I^-\right] = 0 \qquad \forall \delta\Phi^- \in \mathbb{R} \tag{24h}$$

It should be noted that the value of $\Phi^-$ is now part of the solution (cf. formulation of the potentiostatic problem); hence, the additional Eq. (24h) is required.

## 5. Model specification

### 5.1. FE-approximation and implementation in COMSOL Multiphysics®

The numerical implementation is done in the commercial FE software COMSOL Multiphysics version 5.4. The time-incremental weak format of the governing equations presented in Section 4 are setup and solved using the Weak form PDE module and the built-in solver MUMPS (MUltifrontal Massively Parallel sparse direct Solver (MUMPS, 2008)). As to the FE-approximations, triangular Lagrange elements are used for the various primary fields in the fibres and the SBE domains with polynomial order as follows: $\boldsymbol{u}$ quartic (fibre, SBE), $p$ quadratic (SBE), $\varphi$ quadratic (SBE), $\mu_{Li}$ cubic (fibre) and quadratic (SBE), $\mu_X$ quadratic (SBE), $c_{Li}$ cubic (fibre) and quadratic (SBE), $c_X$ quadratic (SBE). By successively raising the polynomial order of the FE-approximation for a given triangulation, a convergence study (not further detailed in this study) shows that the results are reliable and not flawed by discretization errors. The Fully Coupled Approach is used to solve the coupled problem, i.e. the complete system of equations is solved in a monolithic fashion without using any staggering between the different physical mechanisms.

### 5.2. Model geometry and loading conditions

The geometry for the chosen two-dimensional FE-model is illustrated in Fig. 4a. The height ($h_{ext}$) and width ($w_{ext}$) are chosen from Johannisson et al. (2018). The fibre volume fraction ($V_f$) is set to $V_f = 0.45$. The model geometry and element mesh are presented in Fig. 4a.

Although the FE-analysis is two-dimensional, the stress state is three-dimensional due to the assumed stress/strain condition in the $x_3$−direction (along the fibres). We opt for conditions that simulate those which are typical for beam (and plate) kinematics, whereby the $x_3$-direction is the beam axis. The following mechanical loading conditions (in the $x_3$-direction) are considered:

Load(i) Standard plane strain, i.e. $\epsilon_{33}(x_1, x_2, t) = \bar{\epsilon}_{33} = 0$. Postprocessing then gives the field $\sigma_{33}(x_1, x_2, t)$ and the normal force $N_{33}(t)$.

Load(ii) Generalized plane stress, defined by $\epsilon_{33}(x_1, x_2, t) = \bar{\epsilon}_{33}(t)$ and the condition

$$N_{33}(t) := \int_{\Omega} \sigma_{33}(\bullet, t) \, \mathrm{d}S = 0 \tag{25}$$

where we note that $\Omega$ defines a surface in 2D. This is the extra condition that is needed to compute $\bar{\epsilon}_{33}(t)$ as part of the FE-problem. Clearly, postprocessing will provide the field $\sigma_{33}(x_1, x_2, t)$.

With respect to the in-plane mechanical conditions in the $x_1$-direction (Eq. (16a)), we consider the following cases:

Bend(i) In-plane deformations constrained: $\bar{u}_1 = 0$ on $\Gamma_{ext,2} \cup \Gamma_{ext,3}$.

Bend(ii) In-plane deformation $\bar{u}_1$ on $\Gamma_{ext,2} \cup \Gamma_{ext,3}$. This corresponds to the case when in-plane deformations are applied to simulate bending of a structural battery laminate:

$$\bar{u}_1(x_2, t) = \begin{cases} -\bar{\kappa}(t) \frac{w_{ext}}{2} [x_2 - \frac{h_{ext}}{2}], & \text{on } \Gamma_{ext,2} \\ \bar{\kappa}(t) \frac{w_{ext}}{2} [x_2 - \frac{h_{ext}}{2}], & \text{on } \Gamma_{ext,3} \end{cases} \tag{26}$$

A "ramp-loading" in time is introduced, whereby the curvature $\bar{\kappa}(t)$ is parameterized as

$$\bar{\kappa}(t) = \begin{cases} 0, & 0 \le t < t_0 \\ \bar{\kappa}_0 \frac{t - t_0}{t_1 - t_0}, & t_0 \le t < t_1 \\ \bar{\kappa}_0 \frac{t_2 - t}{t_2 - t_1}, & t_1 \le t < t_2 \\ 0, & t \ge t_2 \end{cases} \tag{27}$$

illustrated in Fig. 4b. Here, $\bar{\kappa}_0$ is the magnitude of the applied curvature. The time intervals $t \in [t_0, t_1]$ and $t \in [t_1, t_2]$ represent the time periods in which the mechanical deformation is ramped up and down, respectively. For simplicity the neutral axis is located at the mid-height of the battery cell ($h_{ext}/2$).

For galvanostatic conditions the applied constant (dis)charge current is defined as

$$I^{pre} = i^f m^f \tag{28}$$

where $i^f$ is the applied mass-specific current (intrinsic fibre property) and $m^f$ is the fibre mass of the unit cell (depends on the fibre volume fraction, fibre density and cell size).

### 5.3. Material parameters

The complete set of parameter values used in the analysis is listed in Table B.3 (in Appendix B).

The mechanical properties of the carbon fibres, most notably the elastic constants defining transverse isotropy, are based on experiments by Duan et al. (2020). As to the electrochemical characteristics, the fibre mobilities in the transverse and longitudinal directions are assumed equal (for simplicity): $M_{Li,\perp}(c_{Li}) = M_{Li,\parallel}(c_{Li}) = \eta_{Li} c_{Li}$ where $\eta_{Li}$ is the mobility coefficient of Li in the fibres. This simplification is motivated by the geometric features of the electrode material (fibres) and the studied electrical loading (cf. Hagberg, 2018). The mobility of Li in the fibres is estimated based on the longitudinal diffusion

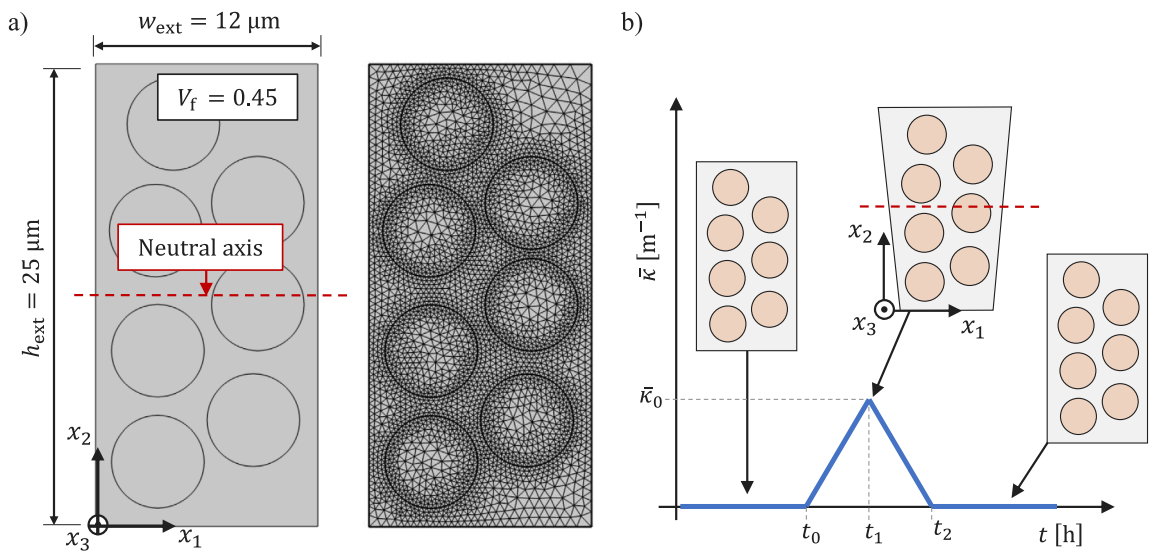


**Fig. 4.** (a) Model geometry and triangular element mesh for the FE-model set-up in COMSOL Multiphysics. (b) Schematic illustration of the in-plane bending of a structural battery laminate, cf. Eq. (26).

coefficient for sized IMS65 carbon fibres at $\tilde{c}_{Li} = 0.05$, cf. Kjell et al. (2013). The reference/standard value $\mu^0_{Li}$ is based on measurements by Kjell et al. (2013). The values of $\alpha^{ch}_{\perp}$, $\alpha^{ch}_{\parallel}$, $i^f$ and $c_{Li,max}$ are chosen on the basis of experiments by Jacques et al. (2013a). It should be noted that these values are correlated and that $i^f$ is defined per kg of fibres in the electrode. For example, $i^f = 168$ A kg$^{-1}$ of fibres corresponds to the electric current needed to discharge the negative half-cell in approximately 1 h (i.e. this can be referred to as *C-rate*=1). The fibre expansion and maximum Li concentration[8] are correlated with the (dis)charge current ($i^f$) based on measurements in Jacques et al. (2013a).

The interface mobility is chosen as $\bar{M} = i_0/[R\theta_0 F]$. For simplicity, we assume that the exchange current density (denoted $i_0$) is constant and is defined in accordance with measurements reported by Kjell et al. (2013). The interface permittivity is expressed as $\bar{\mathcal{E}} = \varepsilon/\delta$, where $\delta$ is the assumed thickness of the electric double layer. The relative permittivity is set to $\varepsilon_r = 10$, cf. Fontanella and Wintersgill (1988), Ganser et al. (2019a). The thickness of the electric double layer is set to 0.5 nm, cf. Ganser et al. (2019a) and Braun et al. (2015).

The intrinsic elastic stiffness of the polymer skeleton of the SBE is set to $E^S = 2.5$ GPa, which corresponds to a conventional polymer system made of vinyl esters, e.g. cf. Kandelbauer et al. (2014). The corresponding intrinsic Poisson's ratio is set to $\nu^S = 0.33$. Moreover, the bulk modulus of the liquid electrolyte is set to $B^F = 1$ GPa, cf. Gor et al. (2014). These elastic properties are used to compute the moduli $B^S$ and $G^S$; thus, the effective moduli $B$ and $G$ for a given porosity. In its turn, the values of $B^S$, $B$, $B^F$ and $\phi$ are used to compute the Biot coefficient $\beta$ and the effective compressibility $\lambda$. For example, for given $B^S = 2.45$ GPa, $B = 0.52$ GPa, $B^F = 1$ GPa and $\phi = 0.4$, we compute $\beta = 0.787$ and $\lambda = 0.56$ GPa$^{-1}$. The mobility coefficients for Li and X in the liquid phase of the SBE are set equal (for simplicity) and are based on measurements by Ihrner et al. (2017). Moreover, the reference/standard value of $\mu$ for Li in the electrolyte (SBE) is set to zero, i.e. $\mu^0_{Li} = 0$. The bulk modulus $B$, shear modulus $G$, permeability $\boldsymbol{K}$ and mobilities $\boldsymbol{M}_{Li}$, $\boldsymbol{M}_X$ of the SBE vary with the porosity $\phi$, and are estimated by means of virtual testing as described in Section 3.2.4. The derived parameters are summarized in Table 1, while the corresponding curve fitting are presented in Fig. 5. It should be noted that the utilized intrinsic properties of the solid and liquid phase of the SBE are intended to replicate the SBE systems studied in Ihrner et al. (2017) and Schneider et al. (2019).

## 6. Results and discussion

### 6.1. Assessment of stress-driven convection

Due to seepage of the liquid electrolyte in the SBE, driven by a pore pressure gradient, convection will occur as an additional transport mechanism. This effect will be assessed in the proposed framework as follows:

- **Conv**: With convection. The problem is solved with full interaction between the transport of electrolyte and transport of ions.
- **NoConv**: Without convection. The electro-chemical problem is solved upon setting $\hat{\boldsymbol{w}} = \boldsymbol{0}$ (cf. Eq. (5b)).

A complete discharge/charge cycle under galvanostatic control (at $i^f = 168$ A kg$^{-1}$ of fibres) and mechanical conditions Load(i) and Bend(i) is considered, and results are presented in Fig. 6. It should be noted that the applied current ($i^f$) corresponds to a (dis)charge time of approximately 1 h (cf. Jacques et al. (2013a)). In this case the battery cell is (dis)charged at a constant current $I^-(t) = I^{pre}$ (cf. Eq. (28)). Moreover, we set $\phi = 0.4$. After the discharge and charge process, respectively, the battery cell is allowed to rest for 500 s (during which the applied current is set to zero: $I^-(t) = 0$). When comparing the results with and without accounting for convection, Fig. 6c and d, we note that the electric potential is only marginally affected by the fluid mass flux. The pore pressure and direction of fluid mass flux at time instances $t = 2610$ s and $t = 6500$ s are presented in Fig. 6e–f, respectively, when convection is accounted for. It appears that both the pore pressure and the fluid mass flux change sign between the discharge and charge processes (as expected).

Fig. 7 presents the electric potential profile for the cell when it is subjected to the same discharge/charge cycle; however, at two different (dis)charge currents: $i^f = 168$ and 58 A kg$^{-1}$ of fibres. It should be noted that 58 A kg$^{-1}$ corresponds to a (dis)charge time of approximately 5 h (Jacques et al., 2013a).[9] From Figs. 7a–b it is clear that the

[8] It should be noted that the maximum Li concentration is estimated as $c_{Li,max} = C^f 3600/F$, where $C^f$ is the assumed specific capacity of the electrode material for a given (dis)charge current.

[9] Note that the maximum Li-concentration ($c_{Li,max} = C^f 3600/F$) in the fibres is altered for the different applied currents ($i^f$) based on the assumed specific capacity $C^f$ provided in Jacques et al. (2013a).

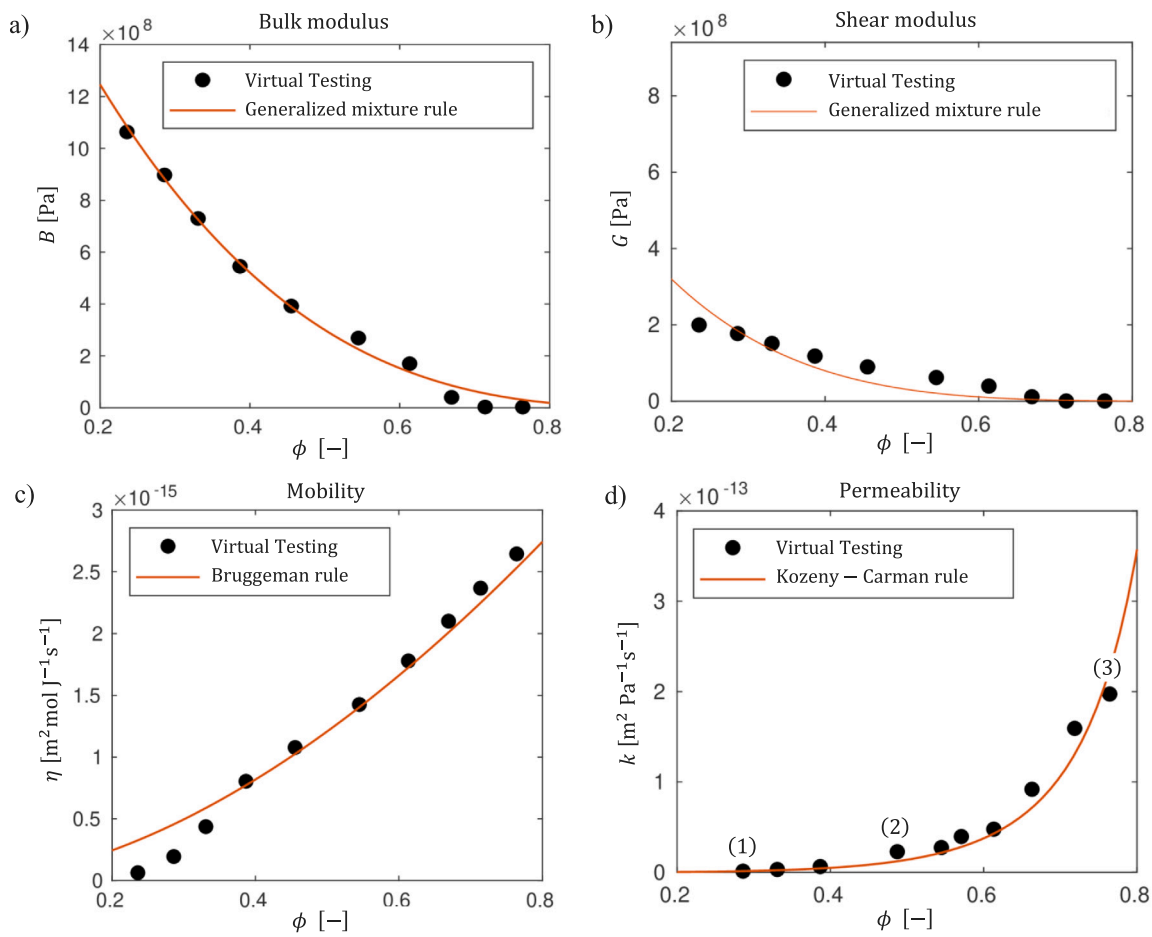


**Fig. 5.** Effective properties of the SBE as function of its porosity $\phi$: (a) bulk modulus $B$, (b) shear modulus $G$, (c) mobility $\eta_\alpha$ and (d) permeability $k$. Each marker • corresponds to a RVE simulation while the line - corresponds to the interpolations rules (cf. Eqs. (9)–(12)). Note that the numbers indicated in (d) correspond to the RVE samples in Fig. 3.

**Table 1**
Derived parameter to approximate the effective properties of the SBE as function of its porosity $\phi$ (cf. Eqs. (8)–(12)).

| Property | Intrinsic value | Unit | $a_1$ | $a_2$ | $a_3$ | $b$ | Eq. | Description |
|---|---|---|---|---|---|---|---|---|
| $B$ | $2.45 \cdot 10^9$ | [Pa] | $B^S$ | 0 | – | 0.330 | (9) | Bulk modulus |
| $G$ | $0.94 \cdot 10^9$ | [Pa] | $G^S$ | 0 | – | 0.207 | (10) | Shear modulus |
| $\eta_\alpha$ | $4 \cdot 10^{-15}$ | [m² mol J⁻¹ s⁻¹] | 0 | $\eta_\alpha^F$ | – | 0.573 | (11) | Mobility |
| $k$ | – | [m² Pa⁻¹ s⁻¹] | – | – | $2.78 \cdot 10^{-14}$ | – | (12) | Permeability |

adopted framework has the ability to capture the relaxation behaviour of the electric potential, which depends on the applied electric loading. Further, it is observed that the shift in electric potential associated with convection is hardly affected by the change in (dis)charge current (Figs. 7c–d). Even though the insertion induced expansion of the fibres is larger in the case of low charge/discharge current ($i^f = 58$ A kg$^{-1}$ of fibres), which will result in a larger pressure gradient inside the cell, the convective contribution to the ion transport is quite insignificant. Moreover, it is observed that the effective stress is orders of magnitude larger compared with the pore pressure under the given conditions (Fig. 7e). In Fig. 7e, it can also be seen that there is a strong interaction between the fluid mass flux and the fibre arrangement/placement. Further, the magnitude of the fluid mass flux ($|\hat{w}|$) is very small which is considered reasonable given the permeability of the SBE (cf. Fig. 5d). However, it must be born in mind that this observation was made in the particular case when no external load has been applied.

### 6.2. Assessment of the SBE characteristics in the presence of convection

Computational results, obtained under galvanostatic conditions (Conv at $i^f = 168$ A kg$^{-1}$ of fibres), are compared for different values of the porosity ($\phi$) of the SBE. From Fig. 8 it is evident that the properties of the SBE affect the electrical and mechanical performance of the structural battery electrode. The effective in-plane mechanical stresses in the SBE are significantly larger in the case of low porosity ($\sigma'_{11}$ and $\sigma'_{22}$ in Fig. 8c–e), which is a consequence of the higher effective stiffness of the SBE for low porosity (cf. Eqs. (9)–(10)). In the case of $\phi = 0.2$, Fig. 8c shows that the tensile effective in-plane stresses approach values of around 5–10 MPa. These stress values can be compared with the average apparent transverse tensile strength of carbon fibre reinforced SBEs (around 11–17 MPa) measured by Xu et al. (2020). Furthermore, the electric potential (Fig. 8b) and the Li-concentration in the SBE ($\tilde{c}_{Li}$ in Figs. 8c–e) are significantly affected by the porosity dependent mobility and permeability of the SBE. Hence, in addition to transport properties of the liquid electrolyte and stiffness of the polymer network, the porosity of the SBE is a crucial design parameter for the combined electro-chemo-mechanical performance.

In Fig. 9 results with convection (Conv) and without convection (NoConv) are compared for the porosity values $\phi = 0.2$ and $\phi = 0.8$, respectively. It is clear that the shift in the electric potential associated with the convective contribution is larger in the case of low porosity

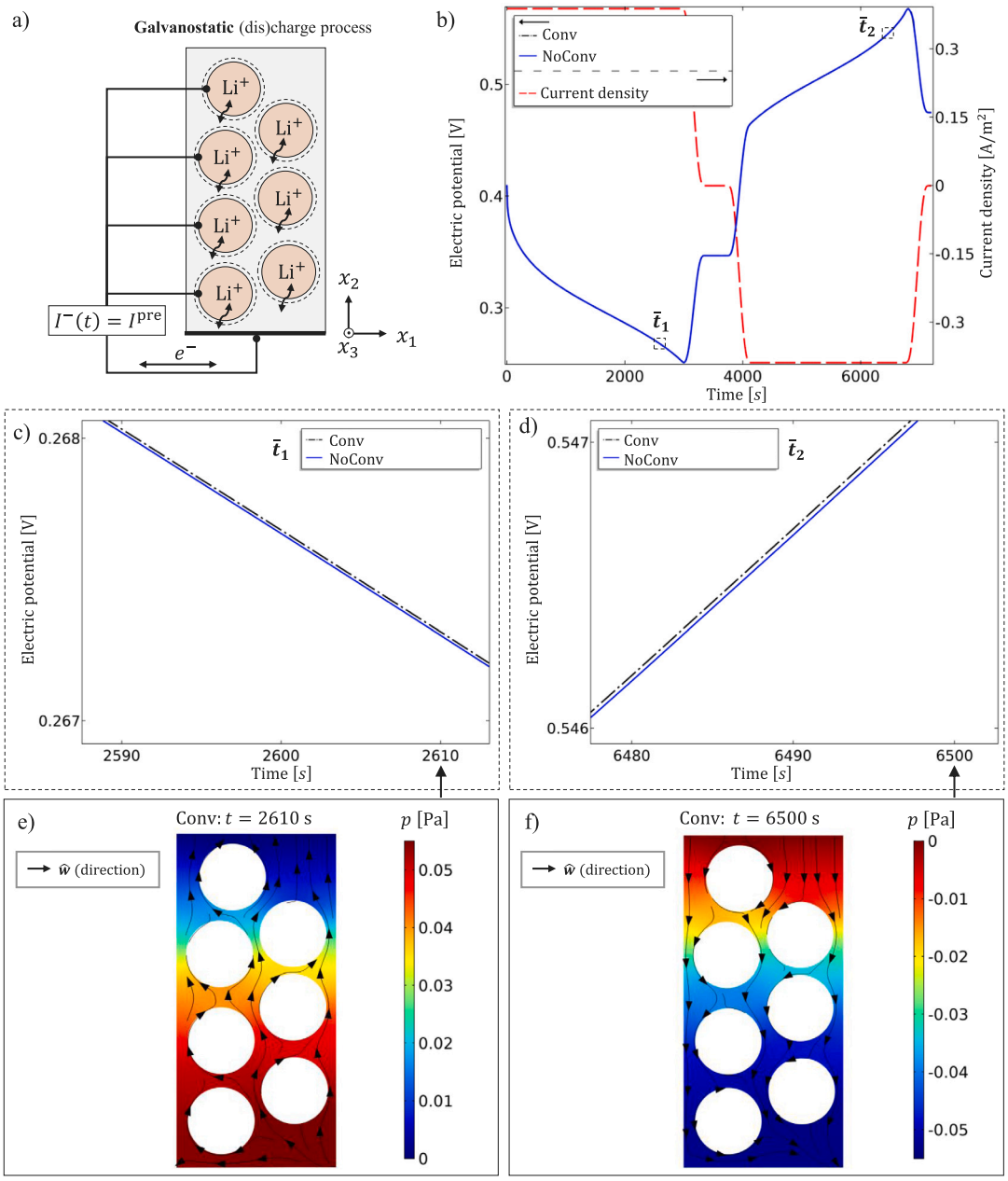


**Fig. 6.** Galvanostatic discharge and charge process with $i^f = 168$ A kg$^{-1}$ of fibres and SBE porosity $\phi = 0.4$. (a) Schematic illustration of process. (b) Cell potential ($\Phi^-$) and current ($I^-$) versus time for Conv: With convection and NoConv: Without convection. (c)–(d) Zoom-in of the electric potential at the two times $\bar{t}_1 \in [2590, 2610]$ s and $\bar{t}_2 \in [6480, 6500]$ s, respectively. (e)–(f) Pore pressure and direction of fluid mass flux for Conv at the time instances $t = 2610$ s and $t = 6500$ s, respectively. Mechanical conditions: Load(i) and Bend(i).

($\phi = 0.2$). This is linked to the effective transport properties of the SBE (cf. Fig. 5).

### 6.3. Assessment of out-of-plane mechanical loading conditions

The influence of two out-of-plane loading conditions (schematically illustrated in Fig. 10a) on the electro-chemical performance are studied.

The computational results in Figs. 10b–c are obtained for the two cases: Conv and NoConv when the cell is subjected to galvanostatic discharge (at $i^f = 168$ A kg$^{-1}$ of fibres and for $\phi = 0.2$). It is observed that the loading conditions have a larger influence on the electric potential than has convection, cf. results in Carlstedt et al. (2020) and Jacques et al. (2013b). However, the shift of the transient part of $\Phi^-(t)$ is found slightly more pronounced for Load(i). This is due to the increased internal stresses (causing a larger pressure gradient) within the SBE for the plain strain loading condition (i.e. Load(i)). Due to the significant difference in stiffness of the constituents, and the fact that the mechanical constraint is applied in the fibre direction, the mechanical load is carried mainly by the fibres. Hence, the SBE only experiences low mechanical stresses which result in similar and minor difference between the two cases: Conv and NoConv, for both the considered loading conditions.

### 6.4. Assessment of in-plane mechanical loading due to bending

The influence of convection in the case of in-plane deformation due to bending of a [90/0] degree structural battery laminate (schematically illustrated in Fig. 11a) is studied. The studied case represents the situation when two electrode laminae are stacked into a laminate with fibre directions perpendicular to each other. When the laminate is bent as schematically illustrated in Fig. 11a the upper lamina will deform as shown. The bending deformation is applied during a short

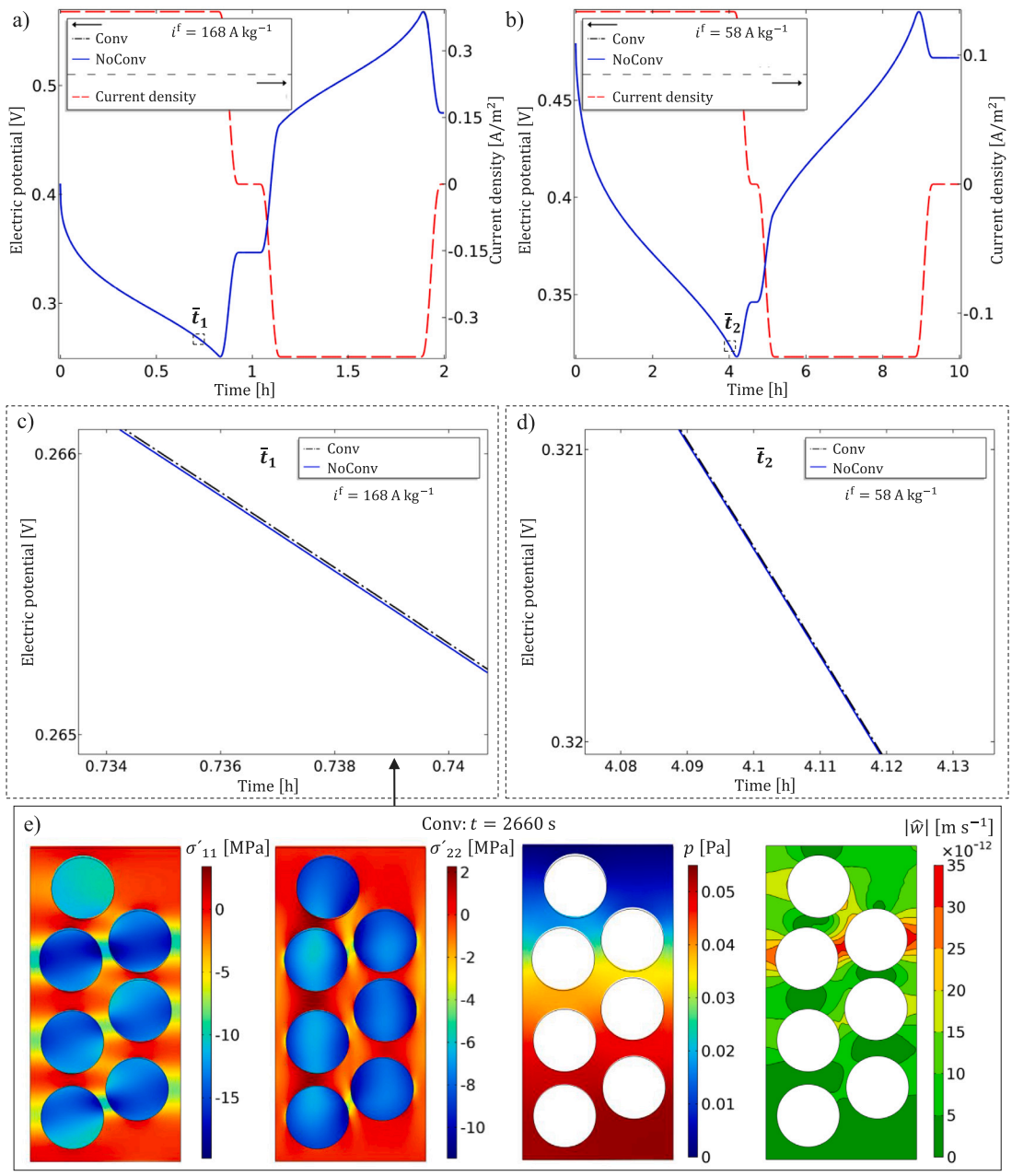


**Fig. 7.** Galvanostatic discharge process at different (dis)charge currents $i^f$ and SBE porosity $\phi = 0.4$. (a)–(b) Cell potential ($\Phi^-$) and current ($I^-$) versus time for $i^f = 168$ and 58 A kg$^{-1}$ of fibres, respectively. (c)–(d) Zoom-in of the electric potential at the two times $\bar{t}_1 \in [0.734, 0.740]$ h and $\bar{t}_2 \in [4.08, 4.13]$ h, respectively. (e) Snapshot of effective stress fields $\sigma'_{11}$, $\sigma'_{22}$, the pore pressure $p$ and the magnitude of the fluid mass flux $|\hat{w}|$ for Conv at $t = 2660$ s ($i^f = 168$ A kg$^{-1}$ of fibres). Mechanical conditions: Load(i) and Bend(i).

discharge process at current densities $i^f = 168$ and 336 A kg$^{-1}$ of fibres, respectively (Fig. 11b). The starting state is defined by setting $\tilde{c}_{Li} = 0.5$, and the current density is then applied and kept constant for a duration of 450 s. In this loading case, denoted Bend(ii) and defined in Section 5.2, the in-plane curvature is applied as a time-ramp as illustrated in Fig. 11b. It should be noted that the magnitude of the applied curvature ($\kappa_0$) is selected such that the assumption of small strains is valid ($|\epsilon_{ij}| \leq 0.06$).

Figs. 11c–d show the electric potential during the discharge process with $i^f = 168$ and 336 A kg$^{-1}$ of fibres, respectively. The studied currents correspond to equivalent (dis)charge times of approximately 1 and 0.3 h, respectively. It is evident that the electric potential is noticeably affected by the convective contribution, in particular for high applied electrical currents. When $i^f = 336$ A kg$^{-1}$ of fibres the shift in the electric potential caused by the applied mechanical load is approximately 3 mV (Fig. 11d). Further, it is evident that the duration and amplitude of mechanical and electrical loading have noticeable influence on the convective contribution to the electro-chemical performance. It should be noted that the electro-chemical performance of a battery during operation is commonly assessed via the measured electric potentials of the cell (e.g. the state of health/charge). Hence, to accurately predict the performance of structural batteries during operation, in particular for applications with highly varying electrical (and possibly also mechanical) loading e.g. electric vehicles (Giordano et al., 2018), it will be important to account for the convective contribution. Moreover, Fig. 11e shows the pore pressure, the fluid mass flux field, and the magnitude of the fluid mass flux ($|\hat{w}|$) for Conv with $i^f = 336$ A kg$^{-1}$ of fibres at the point of maximum mechanical deformation ($t = 300$ s). It is noted that the pore pressure is larger as compared to the case of no external mechanical loading but still several orders of

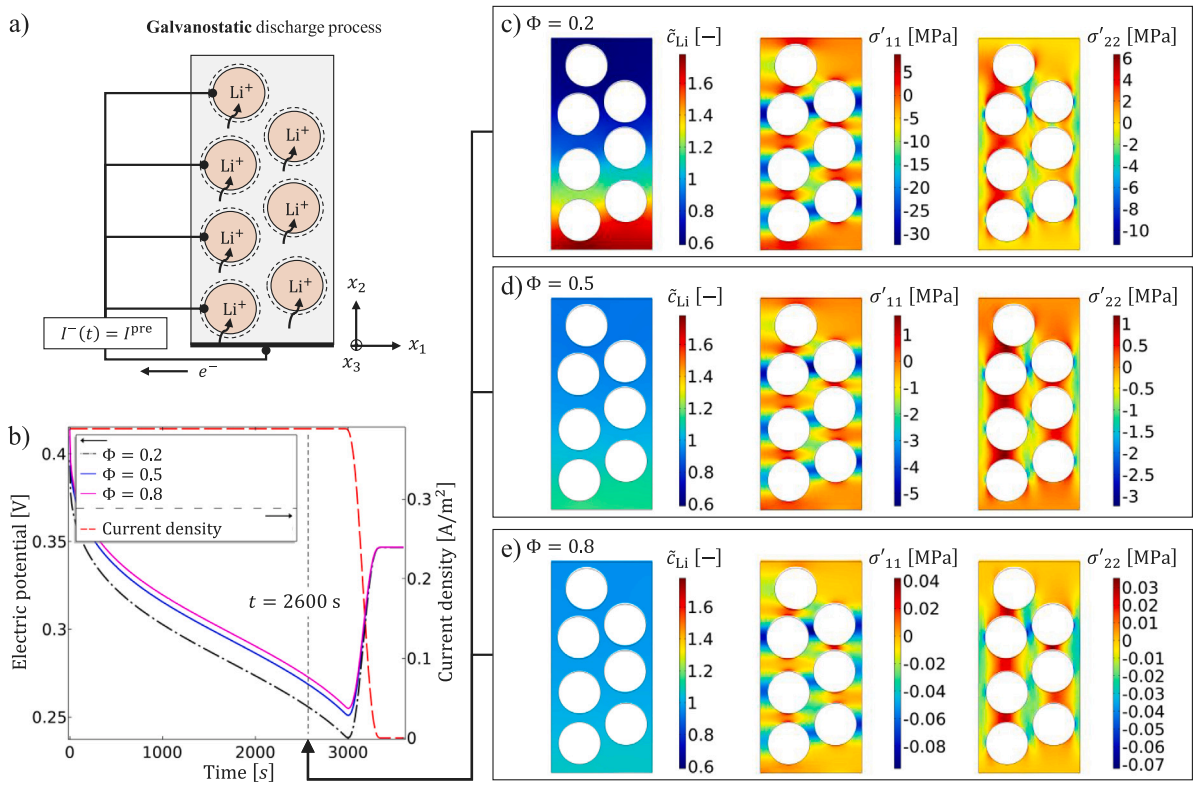


**Fig. 8.** Galvanostatic discharge process for case Conv and the SBE porosity values $\phi = 0.2$, $\phi = 0.5$ and $\phi = 0.8$. (a) Schematic illustration of discharge process. (b) Cell potential ($\Phi^-$) and current ($I^-$) versus time. (c)–(e) Normalized Li-concentration in the electrolyte $\tilde{c}_{Li}$ and effective in-plane stress fields $\sigma'_{11}$ and $\sigma'_{22}$ at $t = 2600$ s for the SBE porosity values $\phi = 0.2$, $\phi = 0.5$ and $\phi = 0.8$, respectively. Mechanical conditions: Load(i) and Bend(i).

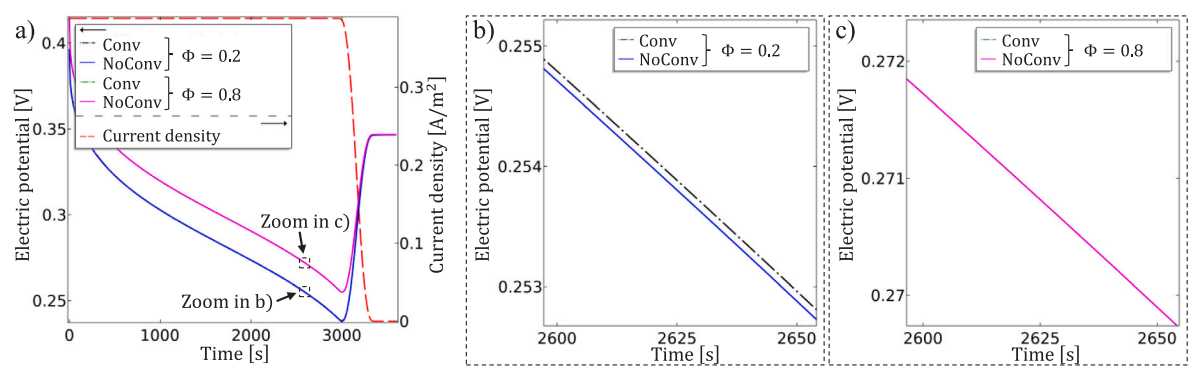


**Fig. 9.** Galvanostatic discharge process for cases Conv and NoConv (i.e. with and without convection) and the SBE porosity values $\phi = 0.2$ and $\phi = 0.8$. (a) Cell potential ($\Phi^-$) and current ($I^-$) versus time. (b)–(c) Zoom-in of the electric potential at the time $t \in [2600, 2650]$ s for SBE porosity values $\phi = 0.2$ and $\phi = 0.8$, respectively. Mechanical conditions: Load(i) and Bend(i).

magnitude smaller than the effective stress components. Further, the fluid mass flux is orders of magnitude larger as compared to the case of no external mechanical loading (cf. Fig. 7e). These results clearly demonstrate that the convective contribution must be accounted for to accurately predict the electro-chemo-mechanical performance when the SBE is subjected to severe in-plane deformation, or when high current pulses are applied.

## 7. Conclusions and outlook to future work

In this paper we present a computational modelling framework to study the electro-chemo-mechanical properties of structural batteries while accounting for the combined action from migration as well as stress-assisted diffusion and convection in the electrolyte. We demonstrate that the framework can be used to simulate continuous electro-chemical charge/discharge processes at different charge rates. The numerical studies reveal that the convective contribution to the mass transport within the SBE (i.e. seepage of the liquid phase) has minor influence on the multifunctional, i.e. electro-chemo-mechanical, performance for loading situations that do not include any externally applied mechanical loading. However, when the mechanical loading causes severe deformation of the SBE, or when large current pulses are applied, the convective contribution has significant influence on the electro-chemical performance. Finally, the numerical results demonstrate that the porosity of the SBE has a profound influence on the multifunctional performance. On the one hand, the electro-chemical performance is impaired whereas the mechanical stresses increase when the porosity is reduced. On the other hand, the electro-chemical performance of the battery cell is improved while the mechanical stresses become smaller for a high-porosity SBE.

Experimental validation/verification of the developed framework is the subject of future work. To assure reliable experimental data, the

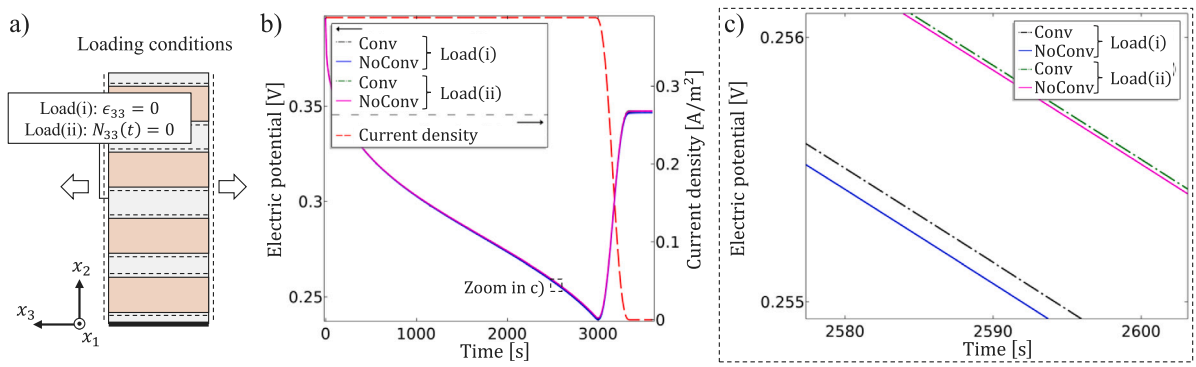


**Fig. 10.** Galvanostatic discharge process for different out-of-plane mechanical loading conditions (SBE porosity $\phi = 0.2$). (a) Schematic illustration of mechanical loading conditions in the fibre direction (i.e. out-of-plane). (b) Cell potential ($\Phi^-$) and current ($I^-$) versus time. (c) Zoom-in of the electric potential at the time $t \in [2580, 2600]$ s. Mechanical conditions: Load(i), Load(ii) and Bend(i).

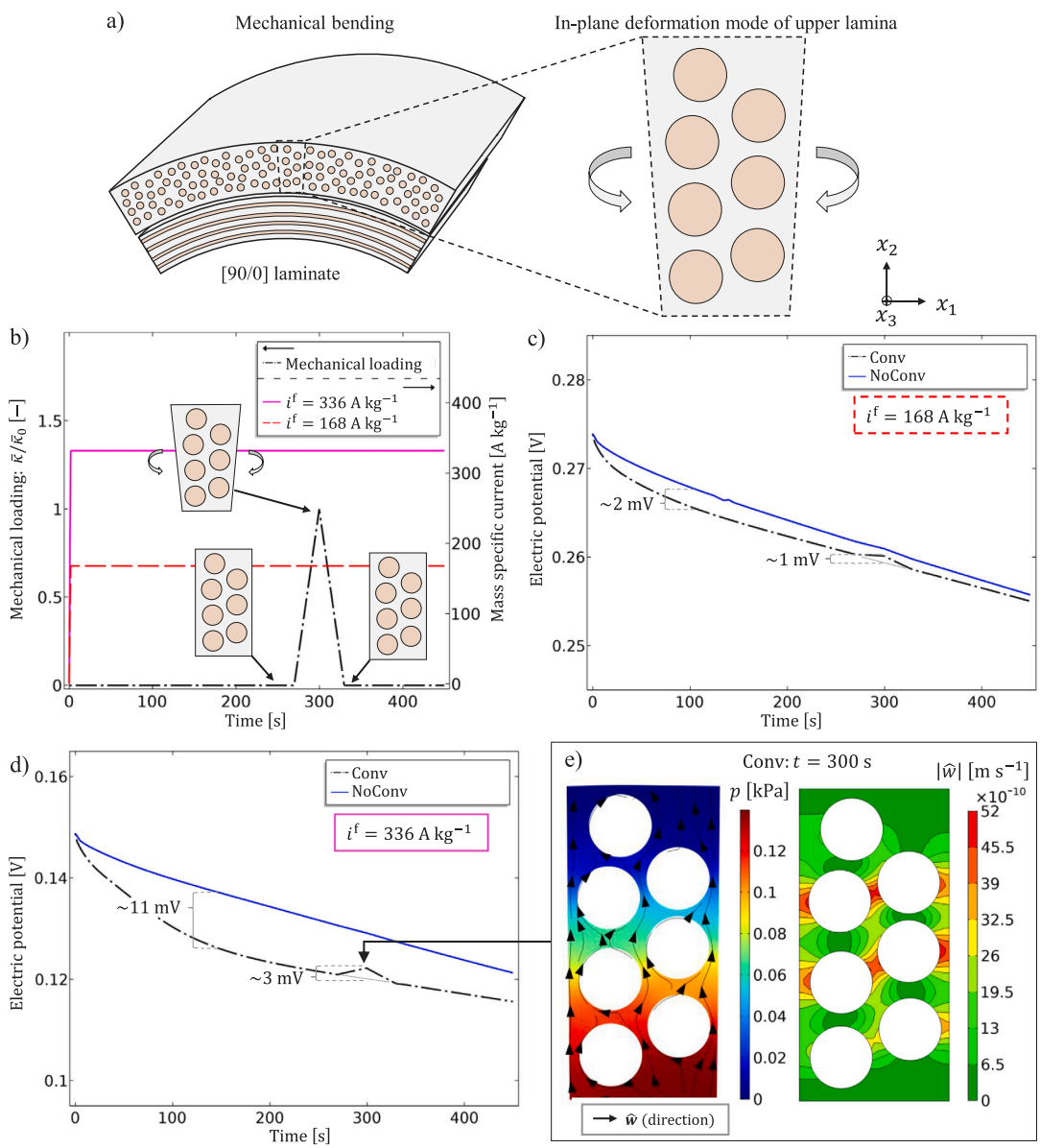


**Fig. 11.** Galvanostatic discharge processes at different discharge current pulses ($i^f$) and in-plane deformation due to bending (SBE porosity $\phi = 0.2$). (a) Schematic illustration of mechanical bending of a [90/0] degree structural battery laminate. (b) Mechanical and electrical loading curves. (c)–(d) Cell potential ($\Phi^-$) versus time for Conv and NoConv at $i^f = 168$ and 336 A kg$^{-1}$ of fibres, respectively. (e) Pore pressure, fluid mass flux field and the magnitude of the fluid mass flux $|\hat{w}|$ for Conv at $t = 300$ s ($i^f = 336$ A kg$^{-1}$ of fibres). Mechanical conditions: Load(i) and Bend(ii).

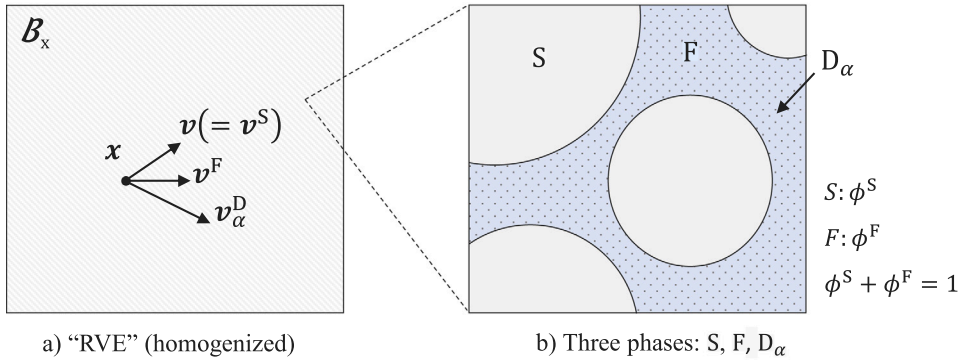


**Fig. A.12.** (a) Schematic illustration: homogenized "RVE" of the considered porous media. (b) The mixture consists of the different phases: S, F, $D_\alpha$ for $\alpha$ = Li,X.

boundary conditions associated with the flow of liquid phase of the SBE need to be controlled. Moreover, since the samples are highly sensitive to moisture and oxygen, the tests must be performed in a controlled environment. Finally, utilizing the developed computational framework for material design optimization of *next generation* structural batteries in terms of its combined electro-chemo-mechanical (i.e. multifunctional) performance is also part of future work.


## Acknowledgements

This project has been funded by the European Union, Clean Sky Joint Undertaking 2, Horizon 2020 under Grant Agreement Number 738085, USAF contract FA9550-17-1-0338, the Swedish National Space Agency, contract 2020-00256, and the Swedish Research Council (VR) Grant no. 2020-05057, which are gratefully acknowledged. The simulations were performed on resources at Chalmers Centre for Computational Science and Engineering (C3SE) provided by the Swedish National Infrastructure for Computing (SNIC).


## Appendix A. Transport of species in a porous medium undergoing finite deformation

### A.1. Preliminaries

Consider a porous SBE with a solid skeleton (S) and pores filled with fluid electrolyte (F) comprising a mixture of species[10] that can carry and transport electric charge (producing a current). It is thus assumed that ions can be transported as dissolved species ($D_\alpha$) only in the fluid by diffusion, migration and convection.[11] Hence, in its very basic form, the entire mixture consists of three principally different phases: S, F, and $D_\alpha$, for $\alpha$ = Li,X, as shown schematically in Fig. A.12.

The reference configuration for the solid skeleton occupying the region $\mathcal{B}_X$ and the deformed configuration $\mathcal{B}_x$ is defined by the mapping $\boldsymbol{x} = \boldsymbol{\varphi}(\boldsymbol{X}) \in \mathcal{B}_x$ for $\boldsymbol{X} \in \mathcal{B}_X$[12] with the deformation gradient $\boldsymbol{F} := \boldsymbol{\varphi} \otimes \boldsymbol{\nabla}_X$ and the Jacobian $J = \det \boldsymbol{F}$. In standard fashion for a classical mixture, we consider substance from all constituents that occupy the same position $\boldsymbol{x} \in \mathcal{B}_x$ at time $t$. However, it is important to note that the reference configurations for S, F, $D_\alpha$ are all different, which means that it is necessary to introduce separate time-variant "deformed configuration functions" $\mathcal{B}_x^S(t)$, $\mathcal{B}_x^F(t)$ and $\mathcal{B}_x^{D_\alpha}(t)$ for the purpose of time-differentiation, although they all share the same "value" $\mathcal{B}_x$ at the considered time $t$. The (spatial) velocity associated with the different phases are conveniently decomposed as follows:

$$\begin{aligned} &\boldsymbol{v}^S := \boldsymbol{v}, \quad \boldsymbol{v}^F = \boldsymbol{v} + \boldsymbol{w} \text{ with } \boldsymbol{w} := \boldsymbol{v}^F - \boldsymbol{v}, \\ &\boldsymbol{v}_\alpha^D = \boldsymbol{v} + \boldsymbol{w} + \boldsymbol{w}_\alpha^D \text{ with } \boldsymbol{w}_\alpha^D := \boldsymbol{v}_\alpha^D - \boldsymbol{v}^F \end{aligned} \tag{A.1}$$

For any given intensive quantity $\boldsymbol{f}^\beta$ associated with the phase $\beta$, we may now compute the time-variation of the extensive quantity contained momentarily within the spatial domain $\mathcal{B}_x^\beta(t)$ as follows (Ehlers, 2002):

$$\frac{\mathrm{d}}{\mathrm{d}t} \int_{\mathcal{B}_x^\beta(t)} \boldsymbol{f}^\beta \, \mathrm{d}V_x = \int_{\mathcal{B}_X} \left[ \partial_t (J \boldsymbol{f}^\beta) + [\boldsymbol{f}^\beta \otimes \Delta \boldsymbol{V}^\beta] \cdot \boldsymbol{\nabla}_X \right] \mathrm{d}V_X \tag{A.2}$$

where $\Delta \boldsymbol{V}^\beta := J \Delta \boldsymbol{v}^\beta \cdot \boldsymbol{F}^{-T}$, with $\Delta \boldsymbol{v}^\beta := \boldsymbol{v}^\beta - \boldsymbol{v}$, is the (contravariant) Piola-transformed relative velocity $\Delta \boldsymbol{V}^\beta$. In Eq. (A.2), and subsequently, $\partial_t(\bullet)$ denotes the "reference time-derivative", i.e. the partial derivative w.r.t. time for $\boldsymbol{X} \in \mathcal{B}_X$ fixed.

### A.2. Balance of mass

The mass of solid and fluid phases contained momentarily within the current configuration $\mathcal{B}_x(t)$[13] are

$$\mathcal{M}^S := \int_{\mathcal{B}_x} \hat{\rho}^S \, \mathrm{d}V_x, \quad \mathcal{M}^F := \int_{\mathcal{B}_x} \hat{\rho}^F \, \mathrm{d}V_x, \quad \mathcal{M}^{D_\alpha} := \int_{\mathcal{B}_x} \hat{\rho}^F c_\alpha \, \mathrm{d}V_x, \quad \alpha = \text{Li,X} \tag{A.3}$$

In the absence of mass transfer between the solid and fluid phases, the individual phase masses are conserved, i.e.

$$\frac{\mathrm{d}}{\mathrm{d}t} \mathcal{M}^\beta = 0, \quad \beta = \mathrm{S, F, D}_\alpha \text{ for } \alpha = \text{Li, X} \tag{A.4}$$

Using the generic result in (A.2), we evaluate

$$\frac{\mathrm{d}}{\mathrm{d}t} \mathcal{M}^S = \int_{\mathcal{B}_X} \partial_t (J \hat{\rho}^S) \, \mathrm{d}V_X \tag{A.5a}$$

$$\frac{\mathrm{d}}{\mathrm{d}t} \mathcal{M}^F = \int_{\mathcal{B}_X} \left[ \partial_t (J \hat{\rho}^F) + [\hat{\rho}^F \boldsymbol{W}] \cdot \boldsymbol{\nabla}_X \right] \mathrm{d}V_X \tag{A.5b}$$

$$\frac{\mathrm{d}}{\mathrm{d}t} \mathcal{M}^{D_\alpha} = \int_{\mathcal{B}_X} \left[ \partial_t (J \hat{\rho}^F c_\alpha) + [\hat{\rho}^F c_\alpha \boldsymbol{W}] \cdot \boldsymbol{\nabla}_X + [\hat{\rho}^F c_\alpha \boldsymbol{W}_\alpha^D] \cdot \boldsymbol{\nabla}_X + R_{X,\alpha} \right] \mathrm{d}V_X \tag{A.5c}$$

where $\boldsymbol{W} := J \boldsymbol{w} \cdot \boldsymbol{F}^{-T}$ and $\boldsymbol{W}_\alpha^D := J \boldsymbol{w}_\alpha^D \cdot \boldsymbol{F}^{-T}$ are the Piola-transformed velocities $\boldsymbol{w}$ and $\boldsymbol{w}_\alpha^D$, respectively. Further, $R_{X,\alpha} := \sum_\beta R_{X,\alpha\beta}$, where we introduced the reaction terms $R_{X,\alpha\beta} = -R_{X,\beta\alpha}$ that represent transfer of ions to species $D_\alpha$ from species $D_\beta$ for $\beta \neq \alpha$. We note the constraint $\sum_\alpha R_{X,\alpha} = \sum_{\alpha,\beta} R_{X,\alpha\beta} = 0$.

[10] In the actual problem formulation, two different types of species are involved in the fluid electrolyte: cation/lithium (Li) and anion (X).

[11] Although it is possible to envision ionic transport in the solid as well, this possibility is ignored for simplicity.

[12] Although reference configurations for F, $D_\alpha$ are conceivable, they have no explicit relevance here.

[13] We do not explicitly indicate the time-variance of the "function" $\mathcal{B}_x^\beta(t)$ for the sake of brevity.

**Table B.2**
List of symbols.

| Symbol | Unit | Description |
|---|---|---|
| $\varphi$ | [V] | Electrical potential |
| $\mu_\alpha$ | [J mol$^{-1}$] | Chemical potential of species $\alpha$ = Li,X |
| $c_\alpha$ | [mol kg$^{-1}$] | Ion concentration of species $\alpha$ = Li,X = molar bulk density of ions divided by bulk density of fluid electrolyte |
| $\tilde{c}_\alpha$ | [–] | Normalized ion concentration of species $\alpha$ = Li,X |
| $\boldsymbol{\sigma}$ | [Pa] | Stress tensor |
| $\boldsymbol{\sigma}'$ | [Pa] | Effective stress tensor |
| $\mathbf{E}$ | [Pa] | Elasticity tensor |
| $\boldsymbol{u}$ | [m] | Displacement field tensor |
| $\boldsymbol{\epsilon}$ | [–] | Strain tensor |
| $\epsilon^{\mathrm{ch}}$ | [–] | Insertion strain |
| $\boldsymbol{\alpha}^{\mathrm{ch}}$ | [kg mol$^{-1}$] | Insertion tensor |
| $\boldsymbol{j}_\alpha$ | [mol m$^{-2}$ s$^{-1}$] | Total ion flux vector of species $\alpha$ = Li,X |
| $\eta_\alpha$ | [m$^2$ mol s$^{-1}$ J$^{-1}$] | Mobility coefficient of species $\alpha$ = Li,X |
| $\boldsymbol{M}_\alpha$ | [mol$^2$ m$^{-1}$ s$^{-1}$ J$^{-1}$] | Mobility tensor for species $\alpha$ = Li,X |
| $\mathcal{K}$ | [S m$^{-1}$] | Ionic conductivity ($\mathcal{K}$=$F^2[\boldsymbol{M}_{\mathrm{Li}} + \boldsymbol{M}_{\mathrm{X}}]$) |
| $\boldsymbol{C}$ | [A Pa$^{-1}$ m$^{-1}$] | Ionic permeability ($\boldsymbol{C}$=$F[c_{\mathrm{Li}} - c_{\mathrm{X}}]\boldsymbol{K}$) |
| $\boldsymbol{\mathcal{E}}$ | [F m$^{-1}$] | Permittivity tensor |
| $\bar{M}$ | [mol$^2$ m$^{-2}$ s$^{-1}$ J$^{-1}$] | Interface mobility |
| $\bar{\mathcal{K}}$ | [S m$^{-2}$] | Interface ionic conductivity ($\bar{\mathcal{K}} = F^2\bar{M}$) |
| $\bar{\mathcal{E}}$ | [F m$^{-2}$] | Interface permittivity |
| $\boldsymbol{i}$ | [A m$^{-2}$] | Current density |
| $\boldsymbol{d}$ | [C m$^{-2}$] | Electric flux density vector |
| $\theta$ | [K] | Temperature |
| $\varepsilon$ | [F m$^{-1}$] | Permittivity |
| $L$ | [Pa] | Lamé's first parameter |
| $G$ | [Pa] | Shear modulus |
| $H_{\parallel}$ | [Pa] | Uniaxial strain modulus |
| $B$ | [Pa] | Bulk modulus |
| $\nu$ | [–] | Poisson's ratio |
| $\Phi^+$ | [V] | Positive electrode potential (set to 0) |
| $\Phi^-$ | [V] | Negative electrode (fibre) potential, controlled or computed |
| $I^-$ | [A] | Circuit current (fibre), controlled or computed |
| $I^{\mathrm{pre}}$ | [A] | Applied/prescribed current (galvanostatic conditions) |
| $\boldsymbol{\sigma}_n$ | [Pa] | Traction |
| $\delta$ | [m] | Thickness of electric double layer |
| $t$ | [s] | Time |
| $\Omega$ | [–] | Domain |
| $\Gamma$ | [–] | Boundary |
| $S$ | [kg m$^{-3}$] | Storage function that represents the volume fraction of pores while accounting for volume change of skeleton |
| $\hat{\boldsymbol{w}}$ | [kg m$^{-2}$ s$^{-1}$] | Fluid mass flux |
| $\rho$ | [kg m$^{-3}$] | Density of carbon fibre |
| $\rho^{\mathrm{F}}$ | [kg m$^{-3}$] | Intrinsic density of fluid (electrolyte) in SBE |
| $p$ | [Pa] | Pore pressure |
| $\boldsymbol{K}$ | [kg m$^{-1}$ Pa$^{-1}$ s$^{-1}$] | Permeability (hydraulic conductivity) tensor |
| $k$ | [m$^2$ Pa$^{-1}$s$^{-1}$] | Permeability coefficient |
| $\phi$ | [–] | Porosity of SBE |
| $a_i$ | [–] | Constant linked to variation in $B$, $G$, $\eta_\alpha$ and $k$ with porosity (SBE) |
| $b$ | [–] | Constant linked to variation in $B$, $G$ and $\eta_\alpha$ with porosity (SBE) |
| $\bar{\kappa}$ | [m$^{-1}$] | Parameterized curvature |
| $i^{\mathrm{f}}$ | [A kg$^{-1}$] | Applied mass-specific current defined per kg of fibres |
| $m^{\mathrm{f}}$ | [kg] | Fibre mass of the unit cell |
| $\beta$ | [–] | Biot coefficient |
| $\lambda$ | [Pa$^{-1}$] | Effective compressibility |

We then obtain the following localized result in the material format:

$$\partial_t(J\hat{\rho}^{\mathrm{S}}) = 0 \tag{A.6a}$$

$$\partial_t(J\hat{\rho}^{\mathrm{F}}) + [\hat{\rho}^{\mathrm{F}}\boldsymbol{W}]\cdot\boldsymbol{\nabla}_{\mathrm{X}} = 0 \tag{A.6b}$$

$$\partial_t(J\hat{\rho}^{\mathrm{F}}c_\alpha) + [\hat{\rho}^{\mathrm{F}}c_\alpha\boldsymbol{W}]\cdot\boldsymbol{\nabla}_{\mathrm{X}} + [\hat{\rho}^{\mathrm{F}}c_\alpha\boldsymbol{W}^{\mathrm{D}}_\alpha]\cdot\boldsymbol{\nabla}_{\mathrm{X}} + R_{\mathrm{X},\alpha} = 0 \tag{A.6c}$$

The relation (A.6c) can be rewritten in a more condensed format

$$\partial_t(J\hat{\rho}^{\mathrm{F}}c_\alpha) + \boldsymbol{J}_\alpha\cdot\boldsymbol{\nabla}_{\mathrm{X}} + R_{\mathrm{X},\alpha} = 0 \tag{A.7}$$

The ion flux $\boldsymbol{J}_\alpha := \boldsymbol{J}^{\mathrm{C}}_\alpha + \boldsymbol{J}^{\mathrm{D}}_\alpha$ is thus split additively into one part due to convection, $\boldsymbol{J}^{\mathrm{C}}_\alpha$, and another due to diffusion and migration, $\boldsymbol{J}^{\mathrm{D}}_\alpha$:

$$\boldsymbol{J}^{\mathrm{C}}_\alpha := \hat{\rho}^{\mathrm{F}}c_\alpha\boldsymbol{W},\ \boldsymbol{J}^{\mathrm{D}}_\alpha := \hat{\rho}^{\mathrm{F}}c_\alpha\boldsymbol{W}^{\mathrm{D}}_\alpha \tag{A.8}$$

Upon using (A.6b) to eliminate $\partial_t(J\hat{\rho}^{\mathrm{F}})$, we may rephrase (A.7) as follows:

$$J\hat{\rho}^{\mathrm{F}}\partial_t c_\alpha + \hat{\rho}^{\mathrm{F}}[\boldsymbol{\nabla}_{\mathrm{X}}c_\alpha]\cdot\boldsymbol{W} + \boldsymbol{J}^{\mathrm{D}}_\alpha\cdot\boldsymbol{\nabla}_{\mathrm{X}} + R_{\mathrm{X},\alpha} = 0 \tag{A.9}$$

It thus follows that the effect of convection will disappear completely when $c_\alpha$ is spatially homogeneous ($\boldsymbol{\nabla}_{\mathrm{X}}c_\alpha = \mathbf{0}$), i.e. even if $\boldsymbol{W} \neq \mathbf{0}$.

Next, we introduce the porosity $\phi$ such that the phase volumes become $\phi^{\mathrm{S}} = 1-\phi$, $\phi^{\mathrm{F}} = \phi$ (and thus $\phi^{\mathrm{S}} + \phi^{\mathrm{F}} = 1$). We also introduce intrinsic phase densities $\rho^{\mathrm{S}}$ and $\rho^{\mathrm{F}}$ and mass-specific concentrations $c_\alpha$, $[c_\alpha] = mol/kg$, such that the (partial) bulk densities become

$$\hat{\rho}^{\mathrm{S}} = \phi^{\mathrm{S}}\rho^{\mathrm{S}} = [1-\phi]\rho^{\mathrm{S}},\quad \hat{\rho}^{\mathrm{F}} = \phi^{\mathrm{F}}\rho^{\mathrm{F}} = \phi\rho^{\mathrm{F}},\quad \hat{\rho}^{\mathrm{D}}_\alpha = c_\alpha\hat{\rho}^{\mathrm{F}} = c_\alpha\phi\rho^{\mathrm{F}} \tag{A.10}$$

whereby (A.6) can be rewritten as

$$\partial_t(J[1-\phi]\rho^{\mathrm{S}}) = 0 \tag{A.11a}$$

$$\partial_t(J\phi\rho^{\mathrm{F}}) + [\phi\rho^{\mathrm{F}}\boldsymbol{W}]\cdot\boldsymbol{\nabla}_{\mathrm{X}} = 0 \tag{A.11b}$$

$$\partial_t(J\phi\rho^{\mathrm{F}}c_\alpha) + [c_\alpha\phi\rho^{\mathrm{F}}\boldsymbol{W}]\cdot\boldsymbol{\nabla}_{\mathrm{X}} + [c_\alpha\phi\rho^{\mathrm{F}}\boldsymbol{W}^{\mathrm{D}}_\alpha]\cdot\boldsymbol{\nabla}_{\mathrm{X}} + \sum_\beta R_{\mathrm{X},\alpha\beta} = 0 \tag{A.11c}$$

Henceforth, we assume the constitutive parametrizations $\rho^{\mathrm{S}} = \rho^{\mathrm{S}}(p,J)$ and $\rho^{\mathrm{F}} = \rho^{\mathrm{F}}(p)$, where $p$ is the intrinsic pressure in the pore liquid. Now, (A.11a) can be integrated to give

$$J[1-\phi]\rho^{\mathrm{S}}(p,J) = [1-\phi_0]\rho^{\mathrm{S}}_0 \tag{A.12}$$

where we used that $J = 1$ for $t = 0$. Hence, we may solve for $\phi(p,J)$ from (A.12) whenever the constitutive function $\rho^{\mathrm{S}}(p,J)$ is known. Upon introducing into (A.11b) and (A.11c), we obtain

$$\partial_t S(p,J) + [X(p,J)\boldsymbol{W}]\cdot\boldsymbol{\nabla}_{\mathrm{X}} = 0 \tag{A.13a}$$

$$\partial_t(S(p,J)c_\alpha) + [c_\alpha X(p,J)\boldsymbol{W}]\cdot\boldsymbol{\nabla}_{\mathrm{X}} + [c_\alpha X(p,J)\boldsymbol{W}^{\mathrm{D}}_\alpha]\cdot\boldsymbol{\nabla}_{\mathrm{X}} = 0 \tag{A.13b}$$

where the storage function $S(p,J)$ and the auxiliary function $X(p,J)$ are defined as

$$S(p,J) := J\phi(p,J)\rho^{\mathrm{F}}(p) = J\,X(p,J) \tag{A.14a}$$

$$X(p,J) := \phi(p,J)\rho^{\mathrm{F}}(p) \tag{A.14b}$$

Clearly, $\phi(p,J)$ as well as $S(p,J)$ and $X(p,J)$ can be expressed explicitly when the parametrizations $\rho^{\mathrm{S}}(p,J)$ and $\rho^{\mathrm{F}}(p)$ are known.

**Linearized model**

Introduce the *approximation* in the form of a *linearized* model in terms of $p$ and the strain $\boldsymbol{\epsilon}$. We linearize at the initial state defined by $\boldsymbol{u} = \boldsymbol{u}_0 = \mathbf{0}$ ($J = J_0 = 1$), $\phi = \phi_0$, to obtain $J \simeq 1 + \boldsymbol{u}\cdot\boldsymbol{\nabla} = 1 + \boldsymbol{\epsilon} : \boldsymbol{I}$. Thus, (A.13) will take the linearized form

$$\partial_t S + \hat{\boldsymbol{w}}\cdot\boldsymbol{\nabla} = 0 \tag{A.15a}$$

$$\partial_t(Sc_\alpha) + \boldsymbol{j}^{\mathrm{C}}_\alpha\cdot\boldsymbol{\nabla} + \boldsymbol{j}^{\mathrm{D}}_\alpha\cdot\boldsymbol{\nabla} + R_\alpha = 0 \tag{A.15b}$$

where $\hat{\boldsymbol{w}} := X\boldsymbol{w}$ is the fluid mass flux, and where the pertinent linearized ion fluxes take the simplified forms:

$$\boldsymbol{j}^{\mathrm{C}}_\alpha := c_\alpha\hat{\boldsymbol{w}},\ \boldsymbol{j}^{\mathrm{D}}_\alpha := c_\alpha X\boldsymbol{w}^{\mathrm{D}}_\alpha \tag{A.16}$$

Next, we elaborate on the appropriate constitutive relations for $S(p,\boldsymbol{\epsilon})$ and $X(p,\boldsymbol{\epsilon})$ that are consistent with the linearized model. From the general expressions in (A.14) we obtain

$$S(p,J) \approx S(p,\boldsymbol{\epsilon}) = \phi_0\rho^{\mathrm{F}}_0 + \left[(\phi'_p)_0\rho^{\mathrm{F}}_0 + \phi_0(\rho^{\mathrm{F}'}_p)_0\right]p + \left[\phi_0 + (\phi'_J)_0\right]\rho^{\mathrm{F}}_0\boldsymbol{\epsilon} : \boldsymbol{I} \tag{A.17a}$$

$$X(p,J) \approx X(p,\boldsymbol{\epsilon}) = \phi_0\rho^{\mathrm{F}}_0 + \left[(\phi'_p)_0\rho^{\mathrm{F}}_0 + \phi_0(\rho^{\mathrm{F}'}_p)_0\right]p + (\phi'_J)_0\rho^{\mathrm{F}}_0\boldsymbol{\epsilon} : \boldsymbol{I} \tag{A.17b}$$

**Table B.3**
Material parameter values.

| Parameter | Value | Unit | Description | Reference |
|---|---|---|---|---|
| $H_{\parallel}$ | 296 | [GPa] | Uniaxial strain modulus fibre | Duan et al. (2020) |
| $L_{\parallel}$ | 5.5 | [GPa] | Lamé's first parameter parallel fibre | Duan et al. (2020) |
| $L_{\perp}$ | 4.7 | [GPa] | Lamé's first parameter perpendicular fibre | Duan et al. (2020) |
| $G_{\parallel}$ | 12.5 | [GPa] | Shear modulus parallel (i.e. $x_3$–$x_{1/2}$ plane) fibre | Duan et al. (2020) |
| $G_{\perp}$ | 9.4 | [GPa] | Shear modulus perpendicular (i.e. $x_1$–$x_2$ plane) fibre | Duan et al. (2020) |
| $L^{\mathrm{S}}$ | 1.82 | [GPa] | Lamé's first parameter for solid phase of SBE | Kandelbauer et al. (2014) |
| $G^{\mathrm{S}}$ | 0.94 | [GPa] | Shear modulus for solid phase of SBE | Kandelbauer et al. (2014) |
| $\eta_{\mathrm{Li}}$ | $5.8 \cdot 10^{-18}$ | [m$^2$ mol s$^{-1}$ J$^{-1}$] | Mobility of Li in fibre (based on diffusion coefficient) | Kjell et al. (2013) |
| $\eta^{\mathrm{F}}_{\mathrm{Li}}$ | $4 \cdot 10^{-15}$ | [m$^2$ mol s$^{-1}$ J$^{-1}$] | Mobility of Li$^+$ in liquid phase of SBE | Ihrner et al. (2017) |
| $\eta^{\mathrm{F}}_{\mathrm{X}}$ | $4 \cdot 10^{-15}$ | [m$^2$ mol s$^{-1}$ J$^{-1}$] | Mobility of X$^-$ in liquid phase of SBE | Ihrner et al. (2017) |
| $\alpha^{\mathrm{ch}}_{\perp}$ | $1.45 \cdot 10^{-3}/1.60 \cdot 10^{-3}/1.85 \cdot 10^{-3}$ | [kg mol$^{-1}$] | Transverse insertion coefficient ($i^{\mathrm{f}}$ = 336/168/58) | Jacques et al. (2013a) |
| $\alpha^{\mathrm{ch}}_{\parallel}$ | $2.68 \cdot 10^{-4}/3.19 \cdot 10^{-4}/4.17 \cdot 10^{-4}$ | [kg mol$^{-1}$] | Longitudinal insertion coefficient ($i^{\mathrm{f}}$ = 336/168/58) | Jacques et al. (2013a) |
| $i^{\mathrm{f}}$ | 336/168/58 | [A kg$^{-1}$] | Applied mass-specific current | Jacques et al. (2013a) |
| $c_{\mathrm{Li,ini}}$ | $5.4 \cdot 10^{-3}$ | [mol kg$^{-1}$] | Initial Li concentration in fibre | – |
| $c_{\mathrm{Li,max}}$ | 3.51/6.27/10.8 | [mol kg$^{-1}$] | Maximum Li concentration in fibre ($i^{\mathrm{f}}$ = 336/168/58) | Jacques et al. (2013a) |
| $c_{\alpha,\mathrm{ref}}$ | 1 | [mol kg$^{-1}$] | Reference/initial concentration of Li$^+$ and X$^-$ in the SBE | Ihrner et al. (2017) and Schneider et al. (2019) |
| $\theta_0$ | 293.15 | [K] | Reference temperature | – |
| $\epsilon_0$ | $8.854 \cdot 10^{-12}$ | [F m$^{-1}$] | Vacuum permittivity | – |
| $\epsilon_r$ | 10 | [–] | Relative permittivity | Fontanella and Wintersgill (1988) and Ganser et al. (2019a) |
| $i_0$ | 1 | [A m$^{-2}$] | Exchange current density | Kjell et al. (2013) |
| $\mu^0_{\mathrm{Li}}$ | $3.86 \cdot 10^4$ | [J mol$^{-1}$] | Reference chemical potential Li in fibre (vs. Li/Li$^+$) | Kjell et al. (2013) |
| $\mu^0_{\alpha}$ | 0 | [J mol$^{-1}$] | Reference chemical potential Li$^+$ and X$^-$ in SBE | – |
| $f_{\alpha}$ | 1 | [–] | Activity coefficient Li$^+$ and X$^-$ in SBE | – |
| $\rho$ | 1850 | [kg m$^{-3}$] | Fibre density | – |
| $\rho^{\mathrm{F}}$ | 1000 | [kg m$^{-3}$] | Intrinsic density of fluid (electrolyte) in SBE | – |
| $\delta$ | $0.5 \cdot 10^{-9}$ | [m] | Thickness of electric double layer | Ganser et al. (2019a) and Braun et al. (2015) |
| $F$ | 96485 | [C mol$^{-1}$] | Faraday's constant | – |
| $R$ | 8.314 | [J K$^{-1}$ mol$^{-1}$] | Gas constant | – |
| $\bar{\kappa}_0$ | $1.6 \cdot 10^3$ | [m$^{-1}$] | Magnitude of applied curvature | – |
| $B^{\mathrm{F}}$ | 1 | [GPa] | Intrinsic bulk modulus liquid phase of SBE | Gor et al. (2014) |

The sensitivities $(\phi'_p)_0$, $(\phi'_J)_0$ are computed in terms of the constitutive tangent moduli $(\rho^{\mathrm{S}'}_p)_0$, $(\rho^{\mathrm{S}'}_J)_0$ and $(\rho^{\mathrm{F}'}_p)_0$ upon differentiation of (A.12) w. r. t. $p$ and $J$, respectively, followed by linearization

$$(\phi'_p)_0 = [1-\phi_0]\frac{(\rho^{\mathrm{S}'}_p)_0}{\rho^{\mathrm{S}}_0} \tag{A.18a}$$

$$(\phi'_J)_0 = [1-\phi_0]\left[\frac{(\rho^{\mathrm{S}'}_J)_0}{\rho^{\mathrm{S}}_0}+1\right] \tag{A.18b}$$

We thus obtain

$$S(p,\boldsymbol{\epsilon}) = \phi_0\rho^{\mathrm{F}}_0 + \rho^{\mathrm{F}}_0\left[[1-\phi_0]\frac{(\rho^{\mathrm{S}'}_p)_0}{\rho^{\mathrm{S}}_0}+\phi_0\frac{(\rho^{\mathrm{F}'}_p)_0}{\rho^{\mathrm{F}}_0}\right]p + \rho^{\mathrm{F}}_0\left[\phi_0+[1-\phi_0][1+\frac{(\rho^{\mathrm{S}'}_J)_0}{\rho^{\mathrm{S}}_0}]\right]\boldsymbol{\epsilon}:\boldsymbol{I} \tag{A.19a}$$

$$X(p,\boldsymbol{\epsilon}) = \phi_0\rho^{\mathrm{F}}_0 + \rho^{\mathrm{F}}_0\left[[1-\phi_0]\frac{(\rho^{\mathrm{S}'}_p)_0}{\rho^{\mathrm{S}}_0}+\phi_0\frac{(\rho^{\mathrm{F}'}_p)_0}{\rho^{\mathrm{F}}_0}\right]p + \rho^{\mathrm{F}}_0[1-\phi_0]\left[1+\frac{(\rho^{\mathrm{S}'}_J)_0}{\rho^{\mathrm{S}}_0}\right]\boldsymbol{\epsilon}:\boldsymbol{I} \tag{A.19b}$$

It remains to introduce explicit values of the constitutive tangent moduli $(\rho^{\mathrm{S}'}_p)_0$, $(\rho^{\mathrm{S}'}_J)_0$ and $(\rho^{\mathrm{F}'}_p)_0$ in terms of measurable parameters. It is possible to derive[14]

$$\frac{(\rho^{\mathrm{S}'}_p)_0}{\rho^{\mathrm{S}}_0} = \left[1-\frac{1}{1-\phi_0}\frac{B}{B^{\mathrm{S}}}\right]\frac{1}{B^{\mathrm{S}}}, \tag{A.20a}$$

$$\frac{(\rho^{\mathrm{S}'}_J)_0}{\rho^{\mathrm{S}}_0} = -\frac{1}{1-\phi_0}\frac{B}{B^{\mathrm{S}}} \tag{A.20b}$$

$$\frac{(\rho^{\mathrm{F}'}_p)_0}{\rho^{\mathrm{F}}_0} = \frac{1}{B^{\mathrm{F}}} \tag{A.20c}$$

where $B^{\mathrm{S}}$ and $B^{\mathrm{F}}$ are the intrinsic bulk modulus of the solid and liquid phase, respectively, whereas $B$ is the effective bulk modulus of the porous material. Finally, the linearized model functions may be formulated quite explicitly as

$$S(p,\boldsymbol{\epsilon}) \approx \rho^{\mathrm{F}}_0\left[\phi_0+\lambda p+\beta\boldsymbol{\epsilon}:\boldsymbol{I}\right] \tag{A.21a}$$

$$X(p,\boldsymbol{\epsilon}) \approx \rho^{\mathrm{F}}_0\left[\phi_0+\lambda p+[\beta-\phi_0]\boldsymbol{\epsilon}:\boldsymbol{I}\right] \tag{A.21b}$$

where

$$\lambda = [1-\phi_0-\frac{B}{B^{\mathrm{S}}}]\frac{1}{B^{\mathrm{S}}}+\phi_0\frac{1}{B^{\mathrm{F}}} \tag{A.22a}$$

$$\beta = 1-\frac{B}{B^{\mathrm{S}}} \tag{A.22b}$$

We note that $\beta$ is the classical Biot coefficient occurring in the so-called "effective stress principle".

[14] These relations are derived under the assumption of a isotropic, homogeneous solid phase with bulk modulus $B^{\mathrm{S}}$, e.g., Wang (2017).

**Special case of intrinsically incompressible solid and fluid phases:**

Now, consider the special case that the solid and fluid phases are intrinsically incompressible. In terms of the chosen linearized model, this state is defined by $B^S = B^F = \infty$, whereby $\lambda = 0$, $\beta = 1$.

## Appendix B. Symbols and parameters

Symbols and parameters used in the analysis presented in this paper are listed in Tables B.2 and B.3.

## References


Asp, L.E., Bouton, K., Carlstedt, D., Duan, S., Harnden, R., Johannisson, W., Johansen, M., Johansson, M., Lindbergh, G., Liu, F., Peuvot, K., Schneider, L.M., Xu, J., Zenkert, D., 2021. A structural battery and its multifunctional performance. Adv. Energy Sustain. Res. 2, 2000093. http://dx.doi.org/10.1002/aesr.202000093.

Asp, L.E., Greenhalgh, E.S., 2014. Structural power composites. Compos. Sci. Technol. 101, 41–61. http://dx.doi.org/10.1016/j.compscitech.2014.06.020.

Asp, L.E., Johansson, M., Lindbergh, G., Xu, J., Zenkert, D., 2019. Structural battery composites: a review. Funct. Compos. Struct. 1, 042001. http://dx.doi.org/10.1088/2631-6331/ab5571.

Bazant, M.Z., 2014. II. Equilibrium Thermodynamics Lecture 8: The Nernst Equation. In: Lecture Notes in 10.626 Electrochemical Energy Systems, Massachusetts Institute of Technology: MIT Open Course Ware, URL: https://ocw.mit.edu/courses/chemical-engineering/10-626-electrochemical-energy-systems-spring-2014/lecture-notes/MIT10_626S14_S11lec08.pdf.

Bower, A.F., Guduru, P.R., Sethuraman, V.A., 2011. A finite strain model of stress, diffusion, plastic flow, and electrochemical reactions in a lithium-ion half-cell. J. Mech. Phys. Solids (ISSN: 0022-5096) 59, 804–828. http://dx.doi.org/10.1016/j.jmps.2011.01.003.

Braun, S., Yada, C., Latz, A., 2015. Thermodynamically consistent model for space-charge-layer formation in a solid electrolyte. J. Phys. Chem. C 119, 22281–22288. http://dx.doi.org/10.1021/acs.jpcc.5b02679.

Bruggeman, D.A.G., 1937. Berechnung verschiedener physikalischer Konstanten von heterogenen Substanzen. III. Die elastischen Konstanten der quasiisotropen Mischkörper aus isotropen Substanzen. Ann. Phys. 421, 160–178. http://dx.doi.org/10.1002/andp.19374210205.

Bucci, G., Chiang, Y.-M., Carter, W.C., 2016. Formulation of the coupled electrochemical-mechanical boundary value problem, with applications to transport of multiple charged species. Acta Mater. 104, 33–51. http://dx.doi.org/10.1016/j.actamat.2015.11.030.

Bucci, G., Swamy, T., Bishop, S., Sheldon, B.W., Chiang, Y.M., Carter, W.C., 2017. The effect of stress on battery-electrode capacity. J. Electrochem. Soc. 164 (4), A645–A654. http://dx.doi.org/10.1149/2.0371704jes.

Cano, Z.P., Banham, D., Ye, S., Hintennach, A., Lu, J., Fowler, M., Chen, Z., 2018. Batteries and fuel cells for emerging electric vehicle markets. Nature Energy 3, 279–289. http://dx.doi.org/10.1038/s41560-018-0108-1.

Carlson, T., 2013. Multifunctional Composite Materials - Design, Manufacture and Experimental Characterisation (Doctoral Thesis). Luleå University of Technology, Luleå, Sweden.

Carlstedt, D., Asp, L.E., 2019. Thermal and diffusion induced stresses in a structural battery under galvanostatic cycling. Compos. Sci. Technol. 179, 69–78. http://dx.doi.org/10.1016/j.compscitech.2019.04.024.

Carlstedt, D., Asp, L.E., 2020. Performance analysis framework for structural battery composites in electric vehicles. Composites B 186, 107822. http://dx.doi.org/10.1016/j.compositesb.2020.107822.

Carlstedt, D., Marklund, E., Asp, L.E., 2019. Effects of state of charge on elastic properties of 3D structural battery composites. Compos. Sci. Technol. 169, 26–33. http://dx.doi.org/10.1016/j.compscitech.2018.10.033.

Carlstedt, D., Runesson, K., Larsson, F., Xu, J., Asp, L.E., 2020. Electro-chemo-mechanically coupled computational modelling of structural batteries. Multifunct. Mater. 3, 045002. http://dx.doi.org/10.1088/2399-7532/abc60d.

Carman, P.C., 1997. Fluid flow through granular beds. Chem. Eng. Res. Des. 75, S32–S48. http://dx.doi.org/10.1016/S0263-8762(97)80003-2.

Doyle, M., Fuller, T.F., Newman, J., 1993. Modeling of galvanostatic charge and discharge of the lithium/polymer/insertion cell. J. Electrochem. Soc. 140, 1526. http://dx.doi.org/10.1149/1.2221597.

Doyle, M., Newman, J., 1995. The use of mathematical modeling in the design of lithium/polymer battery systems. Electrochim. Acta 40, 2191–2196. http://dx.doi.org/10.1016/0013-4686(95)00162-8.

Duan, S., Liu, F., Pettersson, T., Creighton, C., Asp, L.E., 2020. Determination of transverse and shear moduli of single carbon fibres. Carbon 158, 772–782. http://dx.doi.org/10.1016/j.carbon.2019.11.054.

Ehlers, W., 2002. Foundations of multiphasic and porous materials. In: Ehlers, W., Bluhm, J. (Eds.), Porous Media: Theory, Experiments and Numerical Applications. Springer Berlin Heidelberg, Berlin, Heidelberg, pp. 3–86. http://dx.doi.org/10.1007/978-3-662-04999-0_1.

Ekstedt, S., Wysocki, M., Asp, L.E., 2010. Structural batteries made from fibre reinforced composites. Plast. Rubber Compos. 39, 148–150. http://dx.doi.org/10.1179/174328910X12647080902259.

Esan, O.C., Shi, X., Pan, Z., Huo, X., An, L., Zhao, T.S., 2020. Modeling and simulation of flow batteries. Adv. Energy Mater. 10, 2000758. http://dx.doi.org/10.1002/aenm.202000758.

Fontanella, J.J., Wintersgill, M.C., 1988. Low frequency dielectric properties of polyether Electrolytes. Polym. Electrolyte Rev. 2.

Fredi, G., Jeschke, S., Boulaoued, A., Wallenstein, J., Rashidi, M., Liu, F., Harnden, R., Zenkert, D., Hagberg, J., Lindbergh, G., Johansson, P., Stievano, L., Asp, L.E., 2018. Graphitic microstructure and performance of carbon fibre Li-ion structural battery electrodes. Multifunct. Mater. 1, 015003. http://dx.doi.org/10.1088/2399-7532/aab707/meta.

Ganser, M., Hildebrand, F.E., Kamlah, M., McMeeking, R.M., 2019a. A finite strain electro-chemo-mechanical theory for ion transport with application to binary solid electrolytes R. J. Mech. Phys. Solids 125, 681–713. http://dx.doi.org/10.1016/j.jmps.2019.01.004.

Ganser, M., Hildebrand, F.E., Klinsmann, M., Hanauer, M., Kamlah, M., McMeeking, R.M., 2019b. An extended formulation of Butler-Volmer electrochemical reaction kinetics including the influence of mechanics. J. Electrochem. Soc. 166, H167–H176. http://dx.doi.org/10.1149/2.1111904jes.

Giordano, G., Klass, V., Behm, M., Lindbergh, G., Sjöberg, J., 2018. Model-based lithium-ion battery resistance estimation from electric vehicle operating data. IEEE Trans. Veh. Technol. 67, 3720–3728. http://dx.doi.org/10.1109/TVT.2018.2796723.

Gor, G.Y., Cannarella, J., Prévost, J.H., Arnold, C.B., 2014. A model for the behavior of battery separators in compression at different strain/charge rates. J. Electrochem. Soc. 161, F3065–F3071. http://dx.doi.org/10.1149/2.0111411jes.

Grazioli, D., Magri, M., Salvadori, A., 2016. Computational modeling of Li-ion batteries. Comput. Mech. 58, 889–909. http://dx.doi.org/10.1007/s00466-016-1325-8.

Grazioli, D., Verners, O., Zadin, V., Brandell, D., Simone, A., 2019a. Electrochemical-mechanical modeling of solid polymer electrolytes: Impact of mechanical stresses on Li-ion battery performance. Electrochim. Acta 296, 1122–1141. http://dx.doi.org/10.1016/j.electacta.2018.07.234.

Grazioli, D., Zadin, V., Brandell, D., Simone, A., 2019b. Electrochemical-mechanical modeling of solid polymer electrolytes: Stress development and non-uniform electric current density in trench geometry microbatteries. Electrochim. Acta 296, 1142–1162. http://dx.doi.org/10.1016/j.electacta.2018.07.146.

Hagberg, J., 2018. Carbon Fibres for Multifunctional Lithium-Ion Batteries (Doctoral Thesis). Royal Institute of Technology KTH, Stockholm, Sweden.

Hagberg, J., Maples, H., Alvim, K., Xu, J., Johannisson, W., Bismarck, A., Zenkert, D., Lindbergh, G., 2018. Lithium iron phosphate coated carbon fiber electrodes for structural lithium ion batteries. Compos. Sci. Technol. 162, 235–243. http://dx.doi.org/10.1016/j.compscitech.2018.04.041.

Hofmann, T., Westhoff, D., Feinauer, J., Andrä, H., Zausch, J., Schmidt, V., Müller, R., 2020. Electro-chemo-mechanical simulation for lithium ion batteries across the scales. Int. J. Solids Struct. 184, 24–39. http://dx.doi.org/10.1016/j.ijsolstr.2019.05.002.

Ihrner, N., Johannisson, W., Sieland, F., Zenkert, D., Johansson, M., 2017. Structural lithium ion battery electrolytes: Via reaction induced phase-separation. J. Mater. Chem. A 5, 25652–25659. http://dx.doi.org/10.1039/C7TA04684G.

Jacques, E., Hellqvist Kjell, M., Zenkert, D., Lindbergh, G., Behm, M., 2013a. Expansion of carbon fibres induced by lithium intercalation for structural electrode applications. Carbon 59, 246–254. http://dx.doi.org/10.1016/j.carbon.2013.03.015.

Jacques, E., Kjell, M.H., Zenkert, D., Lindbergh, G., 2013b. Piezo-electrochemical effect in lithium-intercalated carbon fibres. Electrochem. Commun. 35, 65–67. http://dx.doi.org/10.1016/j.elecom.2013.07.040.

Johannisson, W., Ihrner, N., Zenkert, D., Johansson, M., Carlstedt, D., Asp, L.E., Sieland, F., 2018. Multifunctional performance of a carbon fiber UD lamina electrode for structural batteries. Compos. Sci. Technol. 168, 81–87. http://dx.doi.org/10.1016/j.compscitech.2018.08.044.

Johannisson, W., Zenkert, D., Lindbergh, G., 2019. Model of a structural battery and its potential for system level mass savings. Multifunct. Mater. 2, 035002. http://dx.doi.org/10.1088/2399-7532/ab3bdd.

Kandelbauer, A., Tondi, G., Goodman, S.H., 2014. Handbook of Thermoset Plastics: 6. Unsaturated Polyesters and Vinyl Esters. Elsevier.

Kjell, M.H., Jacques, E., Zenkert, D., Behm, M., Lindbergh, G., 2011. PAN-based carbon fiber negative electrodes for structural lithium-ion batteries. J. Electrochem. Soc. 158, A1455–A1460. http://dx.doi.org/10.1149/2.053112jes.

Kjell, M.H., Zavalis, T.G., Behm, M., Lindbergh, G., 2013. Electrochemical characterization of lithium intercalation processes of PAN-based carbon fibers in a microelectrode system. J. Electrochem. Soc. 160, A1473–A1481. http://dx.doi.org/10.1149/2.054309jes.

Ladpli, P., Nardari, R., Kopsaftopoulos, F., Chang, F.K., 2019. Multifunctional energy storage composite structures with embedded lithium-ion batteries. J. Power Sources 414, 517–529. http://dx.doi.org/10.1016/j.jpowsour.2018.12.051.

Larché, F.C., Cahn, J.W., 1985. Overview no. 41 The interactions of composition and stress in crystalline solids. Acta Metall. 33, 331–357. http://dx.doi.org/10.1016/0001-6160(85)90077-X.

Liu, P., Sherman, E., Jacobsen, A., 2009. Design and fabrication of multifunctional structural batteries. J. Power Sources 189, 646–650. http://dx.doi.org/10.1016/j.jpowsour.2008.09.082.

Moyer, K., Meng, C., Marshall, B., Assal, O., Eaves, J., Perez, D., Karkkainen, R., Roberson, L., Pinta, C.L., 2020. Carbon fiber reinforced structural lithium-ion battery composite: Multifunctional power integration for CubeSats. Energy Storage Mater. 24, 676–681. http://dx.doi.org/10.1016/j.ensm.2019.08.003.

2008. MUltifrontal Massively Parallel Solver (MUMPS 4.8.4) User's guide. URL: http://mumps.enseeiht.fr/doc/userguide_4.8.4.pdf.

Newman, J., Thomas-Alyea, K.E., 2004. Electrochemical Systems. In: The ECS Series of Texts and Monographs, Wiley.

Newman, J., Tiedemann, W., 1975. Porous electrode theory with battery applications. AIChE J. 21, 25–41. http://dx.doi.org/10.1002/aic.690210103.

Purkayastha, R.T., Mcmeeking, R.M., 2012. An integrated 2-D model of a lithium ion battery : the effect of material parameters and morphology on storage particle stress. Comput. Mech. 50, 209–227. http://dx.doi.org/10.1007/s00466-012-0724-8.

Salvadori, A., Bosco, E., Grazioli, D., 2014. A computational homogenization approach for Li-ion battery cells: Part 1 - Formulation. J. Mech. Phys. Solids 65, 114–137. http://dx.doi.org/10.1016/j.jmps.2013.08.010.

Salvadori, A., Grazioli, D., Geers, M.G.D., 2015a. Governing equations for a two-scale analysis of Li-ion battery cells. Int. J. Solids Struct. 59, 90–109. http://dx.doi.org/10.1016/j.ijsolstr.2015.01.014.

Salvadori, A., Grazioli, D., Geers, M.G.D., Danilov, D., Notten, P.H.L., 2015b. A multiscale-compatible approach in modeling ionic transport in the electrolyte of (Lithium ion) batteries. J. Power Sources 293, 892–911. http://dx.doi.org/10.1016/j.jpowsour.2015.05.114.

Schneider, L.M., Ihrner, N., Zenkert, D., Johansson, M., 2019. Bicontinuous electrolytes via thermally initiated polymerization for structural lithium ion batteries. ACS Appl. Energy Mater. 2, 4362–4369. http://dx.doi.org/10.1021/acsaem.9b00563.

Snyder, J.F., Gienger, E.B., Wetzel, E.D., 2015. Performance metrics for structural composites with electrochemical multifunctionality. J. Compos. Mater. 49, 1835–1848. http://dx.doi.org/10.1177/0021998314568167.

Thomas, J.P., Qidwai, M.A., 2004. Mechanical design and performance of composite multifunctional materials. Acta Mater. 52, 2155–2164. http://dx.doi.org/10.1016/j.actamat.2004.01.007.

Tu, V., Asp, L.E., Shirsova, N., Larsson, F., Runesson, K., Jänicke, R., 2020. Performance of bicontinuous structural electrolytes. Multifunct. Mater. 3, 025001. http://dx.doi.org/10.1088/2399-7532/ab8d9b.

Wan, T.H., Ciucci, F., 2020. Electro-chemo-mechanical modeling of solid-state batteries. Electrochim. Acta 331, 135355. http://dx.doi.org/10.1016/j.electacta.2019.135355.

Wang, H.F., 2017. Theory of Linear Poroelasticity with Applications to Geomechanics and Hydrogeology. Princeton University Press, http://dx.doi.org/10.1515/9781400885688.

Wetzel, E.D., 2004. Reducing weight: Multifunctional composites integrated power, communications, and structure. AMPTIAC Q 8 (4), 91–95, URL: https://citeseerx.ist.psu.edu/viewdoc/download?doi=10.1.1.383.7581&rep=rep1&type=pdf.

Wu, B., Lu, W., 2017. A battery model that fully couples mechanics and electrochemistry at both particle and electrode levels by incorporation of particle interaction. J. Power Sources 360, 360–372. http://dx.doi.org/10.1016/j.jpowsour.2017.05.115.

Wu, B., Lu, W., 2019. A consistently coupled multiscale mechanical–electrochemical battery model with particle interaction and its validation. J. Mech. Phys. Solids 125, 89–111. http://dx.doi.org/10.1016/j.jmps.2018.12.005.

Xu, J., Johannisson, W., Johansen, M., Liu, F., Zenkert, D., Lindbergh, G., Asp, L.E., 2020. Characterization of the adhesive properties between structural battery electrolytes and carbon fibers. Compos. Sci. Technol. 188, 107962. http://dx.doi.org/10.1016/j.compscitech.2019.107962.

Xu, J., Lindbergh, G., Varna, J., 2018a. Carbon fiber composites with battery function: Stresses and dimensional changes due to Li-ion diffusion. J. Compos. Mater. 52, 2729–2742. http://dx.doi.org/10.1177/0021998317752825.

Xu, J., Lindbergh, G., Varna, J., 2018b. Multiphysics modeling of mechanical and electrochemical phenomena in structural composites for energy storage: Single carbon fiber micro-battery. J. Reinf. Plast. Compos. 37, 701–715. http://dx.doi.org/10.1177/0731684418760207.

Xu, R., Yang, Y., Yin, F., Liu, P., Cloetens, P., Liu, Y., Lin, F., Zhao, K., 2019. Heterogeneous damage in Li-ion batteries: Experimental analysis and theoretical modeling. J. Mech. Phys. Solids 129, 160–183. http://dx.doi.org/10.1016/j.jmps.2019.05.003.

Xu, Q., Zhao, T.S., 2015. Fundamental models for flow batteries. Prog. Energy Combust. Sci. 49, 40–58. http://dx.doi.org/10.1016/j.pecs.2015.02.001.

Yin, S., Hong, Z., Hu, Z., Liu, B., Gao, X., Li, Y., Xu, J., 2020. Fabrication and multiphysics modeling of modified carbon fiber as structural anodes for lithium-ion batteries. J. Power Sources 476, 228532. http://dx.doi.org/10.1016/j.jpowsour.2020.228532.

Zhao, Y., Zhao, D., Zhang, T., Li, H., Zhang, B., Zhenchong, Z., 2020. Preparation and multifunctional performance of carbon fiber-reinforced plastic composites for laminated structural batteries. Polym. Compos. 41, 3023–3033. http://dx.doi.org/10.1002/pc.25594.